

Article

Aluminum Microspheres Coated with Copper and Nickel Nanoparticles: Catalytic Activity in the Combustion of Ammonium Perchlorate

Yi Wang ^{1,*} and Xiaolan Song ^{2,*}

¹ School of Materials Science and Engineering, North University of China, Taiyuan 030051, China

² School of Environment and Safety Engineering, North University of China, Taiyuan 030051, China

* Correspondence: wangyi528528@nuc.edu.cn (Y.W.); songxiaolan00@126.com (X.S.)

Abstract: This study employed an in-situ displacement technique to eliminate the oxide layer present on the surface of micron aluminum (μAl). Utilizing the exposed metallic aluminum, we facilitated the displacement of copper and nickel nanoparticles. These nanoparticles, approximately 90 nanometers in size, were densely adhered to the surface of the μAl particles. The elemental composition and structural characteristics of the composite particles were meticulously analyzed using Scanning Electron Microscopy (SEM), X-Ray Diffraction (XRD), Energy Dispersive Spectroscopy (EDS), Vibrating Sample Magnetometry (VSM), and X-Ray Photoelectron Spectroscopy (XPS). Subsequently, thermal analysis and combustion performance assessments were conducted to elucidate the catalytic effects of the composite particles ($[\text{nCu+nNi}]/\mu\text{Al}$) on the thermal decomposition and combustion efficiency of ammonium perchlorate (AP). The results elucidate that the nanoparticles immobilized on the surface of μAl are unequivocally metallic copper (nCu) and metallic nickel (nNi). Following the application of nCu and nNi, the oxidation reaction of μAl accelerated by nearly 400 °C; furthermore, the incorporation of $[\text{nCu+nNi}]/\mu\text{Al}$ raised the thermal decomposition peak temperature of AP by approximately 130 °C. Notably, the thermal decomposition activation energy of raw AP reached as high as 241.7 kJ/mol; however, upon doping with $[\text{nCu+nNi}]/\mu\text{Al}$, this activation energy significantly diminished to 161.4 kJ/mol. The findings of the combustion experiments revealed that both the raw AP and the AP modified solely with μAl were impervious to ignition via the hot wire method. In contrast, the AP doped with $[\text{nCu+nNi}]/\mu\text{Al}$ demonstrated pronounced combustion characteristics, achieving an impressive peak flame temperature of 1851 °C. These results substantiate that the nCu and nNi, when deposited on the surface of μAl , not only facilitate the oxidation and combustion of μAl but also significantly enhance the thermal decomposition and combustion dynamics of ammonium perchlorate. Consequently, the $[\text{nCu+nNi}]/\mu\text{Al}$ composite shows considerable promise for application in high-burn-rate hydroxyl-terminated polybutadiene (HTPB) propellants.



Academic Editor: Jacek Tyczkowski

Received: 12 February 2025

Revised: 1 April 2025

Accepted: 1 April 2025

Published: 4 April 2025

Citation: Wang, Y.; Song, X.

Aluminum Microspheres Coated with Copper and Nickel Nanoparticles: Catalytic Activity in the Combustion of Ammonium Perchlorate. *Catalysts*

2025, *15*, 354. <https://doi.org/10.3390/catal15040354>

Copyright: © 2025 by the authors.

Licensee MDPI, Basel, Switzerland.

This article is an open access article distributed under the terms and conditions of the Creative Commons Attribution (CC BY) license (<https://creativecommons.org/licenses/by/4.0/>).

Keywords: micron Al; surface coating; AP; thermolysis; combustion

1. Introduction

Micro-aluminum (μAl) powder possesses distinct advantages, characterized by its high density and substantial heat release during combustion, which render it invaluable in diverse applications such as propellants, explosives, and pyrotechnics [1–5]. The incorporation of μAl into solid rocket propellants can markedly enhance their specific impulse [6]. Furthermore, when μAl is added to composite explosives, it significantly elevates the heat

generated during detonation and markedly enhances their energy output [7]. Historically, explosives containing μ Al were predominantly employed in underwater munitions; however, with the advent and progression of thermobaric weapons, the utilization of μ Al in these advanced explosive formulations has seen substantial growth [8]. Concurrently, the introduction of μ Al in pyrotechnics has also been shown to enhance their visual and auditory effects [9–11].

Nevertheless, in the case of μ Al, the oxidation process is not only impeded by its remarkable thermodynamic stability but also significantly constrained by the structural attributes of the oxide layer enveloping the surfaces of μ Al particles. Typically, Al_2O_3 manifests in five distinct polymorphs: amorphous, theta, delta, gamma, and alpha [12]. Among these, theta- Al_2O_3 and delta- Al_2O_3 are characterized by their inherent instability. These crystal phases undergo transformative interconversion with rising temperatures, during which their crystalline structures—particularly density—experience substantial alterations [12]. At ambient temperature, a dense layer of amorphous alumina envelops the surface of μ Al, effectively isolating the aluminum metal from atmospheric oxygen. As the temperature ascends, amorphous Al_2O_3 progresses towards crystallization, evolving into various crystalline alumina phases. In the differential scanning calorimetry (DSC) analysis, each pronounced oxidation event, denoted by an exothermic peak, is attributable to the transformations occurring within the Al_2O_3 layer. Trunov et al. [12] elucidated that in atmospheric conditions, within the temperature range of 300 °C to 1450 °C, the oxidation of μ Al undergoes three distinctly exothermic processes. Each of these heat-release events is attributed to the crystallization—or transformation—of alumina on the μ Al surface. Such crystalline transformations signify a considerable alteration in the density of the alumina layer. As the temperature ascends, the density of the alumina layer increases substantially. When the mass of the oxide layer remains constant, a pronounced increase in density necessitates the rupture of the oxide layer, consequently exposing the reactive elemental aluminum to the atmosphere. This exposure leads to rapid oxidation by atmospheric oxygen, culminating in a significant release of heat. The oxidation phenomenon associated with μ Al has garnered widespread recognition within the academic community [13–16]. These intricate phase transition processes fundamentally underpin the diminished reactivity of μ Al. Consequently, it is only through the modification of this oxide layer that we can substantially enhance the thermal reactivity of μ Al.

Researchers have demonstrated that the application of organic fluorides, specifically polytetrafluoroethylene [17]; carbon-based materials such as carbon and graphene oxide [18,19]; and nanoscale transition metal oxides (including Co_3O_4 , Fe_2O_3 , ZnO , etc.) [20], alongside nanoscale metals [21–24], to coat the surface of micron-sized aluminum (μ Al) particles can considerably enhance their thermal reactivity. Notably, for μ Al, the incorporation of transition metal particles, such as copper [25], cobalt [26], nickel [27], and iron [28], significantly augments the thermal oxidation efficiency of μ Al. Consequently, transition metal nanoparticles assume a pivotal role in the oxidation process of μ Al. Initially, these metallic nanoparticles displace the Al_2O_3 coating that typically enshrouds the μ Al particles. As the temperature escalates, these nanoparticles are preferentially oxidized into their respective metal oxides at lower temperatures, concurrently releasing a measurable amount of heat. Subsequently, at low temperatures, these oxides are readily reducible through interaction with aluminum (a form of thermite reaction), owing to their proximity to the metallic aluminum. The temperature at which this reduction occurs is significantly lower than the phase transition temperature of the alumina layer, thereby considerably enhancing the oxidation process of micro-aluminum (μ Al). Furthermore, at reduced temperatures, these thermite reactions also liberate heat, further facilitating the oxidation of μ Al. In essence, the presence of nanoparticle metal coatings on the surface of μ Al alters

its oxidation mechanism, rendering the oxidation of aluminum more facile. Consequently, as indicated by the DSC traces, we observe that the oxidation of nCu/μAl after coating yields a greater heat generation and an increased heat flux compared to uncoated μAl [29]. Current experimental investigations have demonstrated that the application of nano-sized copper (Cu) and nickel (Ni) coatings on μAl dramatically enhances the thermal reactivity of μAl powder. For instance, within the nCu/μAl-WO₃ system, an excess of oxidizer leads to a maximum heat release that attains 86% of the theoretical value, representing a 1.54-fold increase compared to the uncoated material. Similarly, in the nNi/μAl-SnO₂ system, an increase in the concentration of nano-sized nickel corresponds with a proportional rise in the system's heat release [30]. Therefore, in the pursuit of enhancing the oxidation efficiency of μAl, it is plausible to apply a coating of nano-sized copper or nickel onto the surfaces of μAl particles. The pertinent question that arises is this: given that the catalytic influence of these metallic particles on the thermal decomposition of ammonium perchlorate (AP) has been established, what is the significance of this investigation? This leads us to our main inquiry: what are the advantages of utilizing bimetallic nanoparticles to coat μAl?

Indeed, the implementation of bimetallic coatings to encapsulate μAl represents a significant innovation and advancement in the preparation process. The traditional methodology, which relies solely on single metal coatings, is inadequate for achieving bimetallic encapsulation of μAl. When two transition metal chlorides or nitrates are concurrently dissolved in deionized water, they experience rapid hydrolysis. Thus, the selection of an appropriate chelating agent is imperative for stabilizing these metals. Through extensive experimental investigation, we have discovered that the incorporation of EDTA-2Na ($C_{10}H_{14}N_2Na_2O_8$) effectively stabilizes elevated concentrations of copper and nickel ions, thereby preventing hydrolysis. Consequently, this outcome is the culmination of numerous experiments, representing a significant technological endeavor fraught with challenges. Nonetheless, beyond the synthesis of [nCu+nNi]/μAl, the paramount importance of this study resides in the potential of bimetallic materials to exert a synergistic catalytic influence that enhances the thermal decomposition or combustion efficiency of ammonium perchlorate when employed as a fuel. This synergistic catalytic effect is anticipated to surpass the efficacy exhibited by individual metal catalysts.

Now, let us examine another research objective of this article, specifically concerning ammonium perchlorate. It is well-established that AP is the most prevalent oxidizer utilized in solid propellants, exhibiting an impressive oxygen balance of approximately +34%. Notably, the combustion of ammonium perchlorate results solely in gaseous products, which imparts propellants utilizing AP as the oxidizer with a superior specific impulse when contrasted with those incorporating potassium nitrate, ammonium nitrate, or potassium perchlorate as oxidizers [31–33]. Nonetheless, ammonium perchlorate is encumbered by a significant drawback: its thermal decomposition temperature is considerably elevated, typically exceeding 430 °C. This limitation engenders notable kinetic deficiencies in the combustion of AP-based propellants. Consequently, over the past two decades, researchers have endeavored to synthesize various materials aimed at reducing the thermal decomposition temperature of AP and enhancing the burn rate of AP-based propellants [34–40]. In this discussion, we shall refrain from reiterating the findings of prior studies. Notably, certain investigations have demonstrated that the incorporation of nano-copper (Cu) and nano-nickel (Ni) markedly lowers the decomposition temperature of AP by 130.2 °C and 112.9 °C, respectively [23,27]. These results signify that nano-Cu and nano-Ni serve as effective catalysts for enhancing the thermolysis of AP, with nano-Cu exhibiting the most pronounced catalytic activity, closely followed by nano-Ni. This observation prompts us to revisit the pivotal question: what is the significance of this research? Indeed, the hallmark of this study resides in the innovative application of a novel methodology for the

concurrent deposition of nano-sized copper (Cu) and nickel (Ni) onto the surface of micron-scale aluminum (μAl). This approach facilitates a comprehensive investigation into their synergistic catalytic effects on the thermal decomposition and combustion performance of ammonium perchlorate. The endeavor aspires to achieve a triad of objectives: enhancing the oxidation efficiency of μAl , optimizing the thermal decomposition efficiency of AP, and improving the dispersibility of the nanocatalysts. It is also imperative to acknowledge that this research represents a significant progression, building upon the foundational work established in prior investigations.

2. Results and Discussion

2.1. Characterization of $[n\text{Cu}+n\text{Ni}]/\mu\text{Al}$

The micro-morphology and structural characteristics of the synthesized $[n\text{Cu}+n\text{Al}]/\mu\text{Al}$ composite particles were meticulously investigated. Initially, the scanning electron microscopy (SEM) images and energy-dispersive X-Ray spectroscopy (EDS) spectra of the composite particles are presented in Figure 1. Figure 1a–d reveals that the μAl particles exhibit remarkable uniformity in size, with an approximate diameter of 20 μm . Furthermore, the surface of each μAl particle is intricately adorned with a layer of diminutive nanoparticles measuring approximately 90 to 100 nm. To elucidate the elemental composition of the nanoparticles that coat the surface of μAl , we performed EDS analysis on the composite particles, as illustrated in Figure 1e–i. It is evident that the composite particles consist of four elemental constituents: aluminum (Al), copper (Cu), nickel (Ni), and oxygen (O). These elements are homogeneously distributed across the surface of the μAl spheres. Notably, the green hue associated with aluminum is the most pronounced, suggesting that the aluminum originates from the elemental Al beneath the coating layer. While the concentration of oxygen is relatively low, its presence indicates that some degree of oxidation of aluminum, nickel, or copper has occurred during the synthesis process. The distributions of copper and nickel on the surface of the microspheres exhibit remarkable uniformity, and their intense coloration signifies that these metals, in a specific valence state, are uniformly deposited upon the μAl particles.

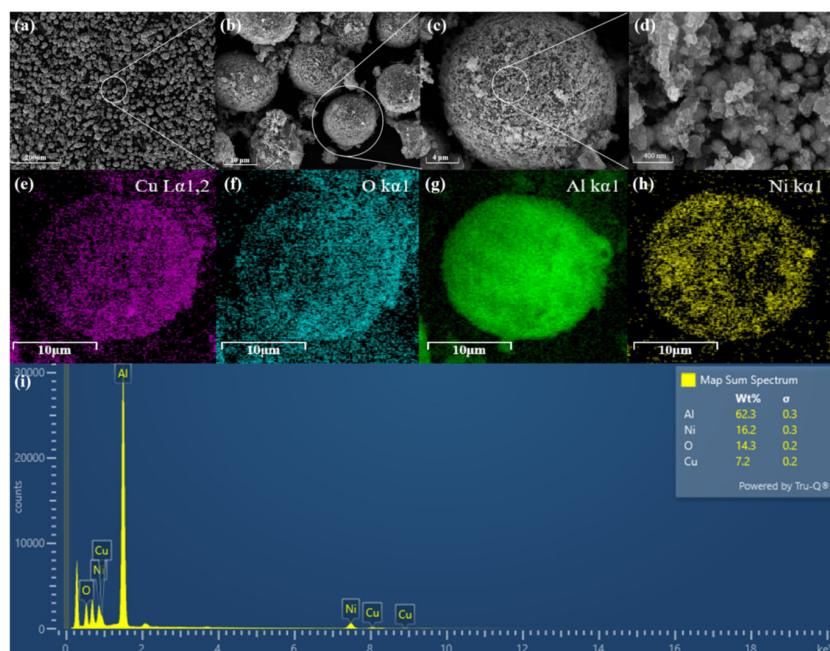


Figure 1. SEM images and EDS spectrum of $[n\text{Cu}+n\text{Ni}]/\mu\text{Al}$: (a–d) SEM images of $[n\text{Cu}+n\text{Ni}]/\mu\text{Al}$; (e–h) Element mapping corresponding to $[n\text{Cu}+n\text{Ni}]/\mu\text{Al}$; (i) Elemental characterization of $[n\text{Cu}+n\text{Ni}]/\mu\text{Al}$.

In our experimental design, we strategically aimed to coat the surface of μ Al with metallic nano-copper and nano-nickel. Consequently, we performed X-Ray diffraction (XRD) analysis on the $[n\text{Cu}+n\text{Ni}]/\mu\text{Al}$ composite particles, with the results illustrated in Figure 2a,b. The XRD patterns reveal a substantial presence of metallic aluminum within the composite particles; however, no diffraction peaks corresponding to aluminum oxide were observed. It is paramount to note that the absence of Al_2O_3 peaks does not entirely exclude the possibility of aluminum oxide forming on the μAl surface, as the aluminum oxide produced at ambient conditions is typically amorphous in nature. Clearly defined diffraction peaks associated with both copper and nickel metals are observed. It is noteworthy that the total mass of the Cu and Ni coating we devised amounts to 5 wt.%. Furthermore, the XRD apparatus employed in this study was a standard X-Ray diffractometer, which effectively identified the presence of metallic copper and metallic nickel. This finding suggests that the nanoparticles adhering to the surface of μAl primarily comprise a blend of metallic nanoparticles of copper ($n\text{Cu}$) and nickel ($n\text{Ni}$), rather than their respective oxides, CuO and NiO .

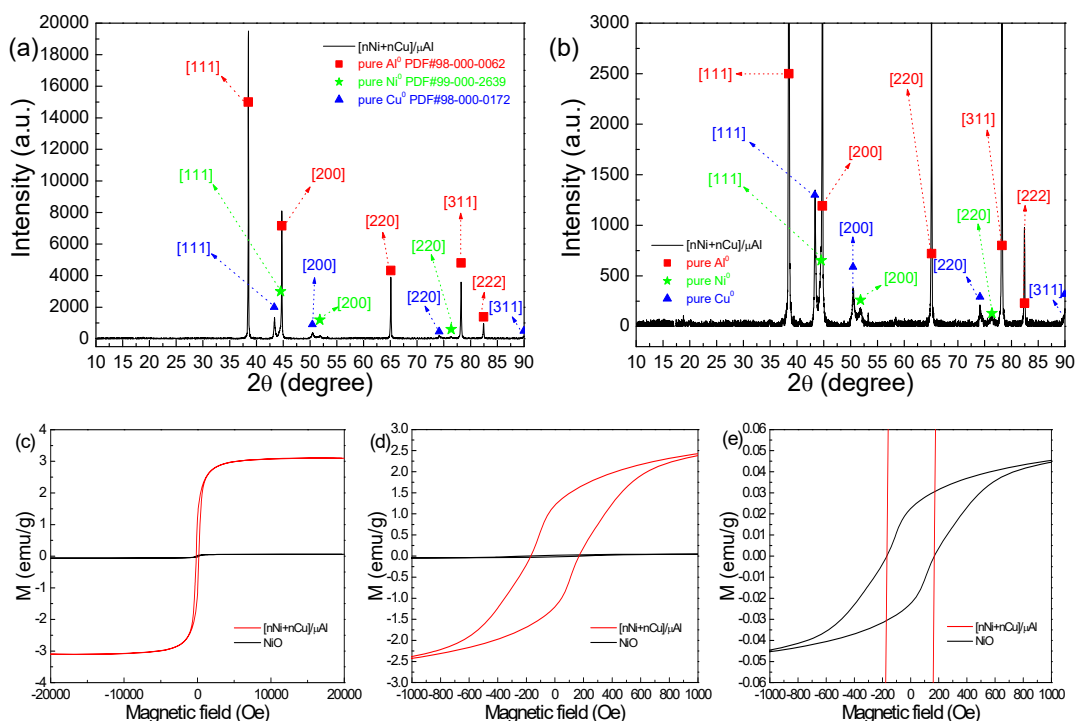


Figure 2. XRD patterns (a,b) and magnetic hysteresis loop (c–e) of $[n\text{Cu}+n\text{Ni}]/\mu\text{Al}$; (b) is the enlarged view of (a); (d,e) are the enlarged views of (c).

It is well established that in systems containing aluminum, oxygen, copper, and iron, both aluminum and aluminum oxide exhibit no ferromagnetic properties, while copper and copper oxide similarly lack ferromagnetism. Nickel oxide demonstrates only exceptionally weak ferromagnetism; conversely, it is metallic nickel that exhibits robust ferromagnetic characteristics. To elucidate the magnetic properties of the synthesized composite particles, we employed Vibrating Sample Magnetometry (VSM) analysis, the results of which are illustrated in Figure 2c–e. Figure 2c reveals that the $[n\text{Cu}+n\text{Ni}]/\mu\text{Al}$ composite particles manifest two distinct VSM curves, indicating the presence of two ferromagnetic substances: one exhibiting strong magnetism and the other weak magnetism. In Figure 2d, the prominent VSM curve displays a significant ferromagnetic response, complete with a discernible coercive force, aligning closely with findings documented in the literature [41]. Undoubtedly, nickel oxide exhibits a degree of ferromagnetism, as illustrated in Figure 2e.

However, its ferromagnetic characteristics are not pronounced; indeed, it demonstrates only weak magnetism in the presence of an external magnetic field, characterized by a low coercive force when the external field is absent [42]. Notably, the composite particles synthesized in this investigation maintain a discernible residual magnetic field even after the external magnetic field dissipates. This behavior closely resembles the hysteresis loop observed in metallic nickel rather than that of nickel oxide [43]. In Figure 2c, the black line delineates the VSM curve of nickel oxide, which aligns closely with findings reported in the literature [42]. The presence of nickel oxide suggests that a minor degree of oxidation has transpired on the surface of the metallic nickel. The VSM curve further reveals that the concentration of NiO is remarkably low. The ferromagnetic behavior, as denoted by the red coloration in Figure 2c, arises from the presence of metallic nano-nickel, confirming the VSM spectrum's indication of metallic nickel's existence. Moreover, the XRD patterns illustrated in Figure 2a,b corroborate the presence of metallic copper. Consequently, these findings suggest that the structure of the $[n\text{Cu}+n\text{Ni}]/\mu\text{Al}$ composite particles consists of a mixture of copper and nickel nanoparticles densely coated on the surface of μAl . This configuration effectively mitigates the restrictive influence of the original Al_2O_3 layer on the oxidation of metallic aluminum.

Figure 3 presents the X-Ray photoelectron spectroscopy (XPS) data of the composite $(n\text{Cu}+n\text{Ni})/\mu\text{Al}$. Panel 3a displays the comprehensive XPS spectrum, while panels 3b to 3e delineate the fine spectra corresponding to O1s, Al2p, Ni2p, and Cu2p, respectively. All spectra have been calibrated using the C1s peak at 285.0 eV as a reference. The XPS results appear rather discouraging. As illustrated in Figure 3b, the oxygen content within $(n\text{Cu}+n\text{Ni})/\mu\text{Al}$ is attributable to the surface oxides of aluminum, copper, and nickel powders, suggesting that the surface of $(n\text{Cu}+n\text{Ni})/\mu\text{Al}$ is coated with their respective oxides. Notably, the XPS peak area associated with alumina is the most pronounced, indicating that the predominant source of oxygen is Al_2O_3 , a result of the considerable proportion of μAl present in the $(n\text{Cu}+n\text{Ni})/\mu\text{Al}$ composite. According to Figure 3c, the characteristic peak of Al 2p observed in $(n\text{Cu}+n\text{Ni})/\mu\text{Al}$ arises from the presence of Al_2O_3 . Figure 3d,e presents the X-Ray Photoelectron Spectroscopy (XPS) characteristic peaks corresponding to typical NiO and CuO, respectively. The aforementioned XPS findings unequivocally indicate the presence of significant metal oxides on the surface of $(n\text{Cu}+n\text{Ni})/\mu\text{Al}$. This phenomenon is expected, given that metallic nCu, nNi, and μAl are readily susceptible to oxidation upon exposure to oxygen in the atmosphere or aqueous solutions with a pH value below 7. This outcome further underscores the importance of performing XPS analyses. Three key factors contribute to this observation. Firstly, elemental copper and nickel, which have been reduced through interaction with elemental aluminum, have indeed experienced partial oxidation in either the solution or the ambient atmosphere. Secondly, prior to conducting the XPS assessment, the samples were not subjected to argon plasma polishing, thereby allowing the oxide layers on the surfaces of elemental copper, nickel, and aluminum to remain intact. Thirdly, it is important to note that X-Ray photoelectron spectroscopy (XPS) functions differently from energy-dispersive X-Ray spectroscopy (EDS) and X-Ray diffraction (XRD). XPS is limited to probing the surface of materials to a depth of only 1 to 3 nanometers. However, we posit that at least 5 nanometers of the surface of the nano-copper and nano-nickel synthesized in this investigation have undergone oxidation to form copper oxide and nickel oxide. It is noteworthy that, as illustrated by the scanning electron microscopy (SEM) images, the dimensions of the nano-copper and nano-nickel produced in this study are approximately 90 nanometers. Consequently, the absence of spectral peaks corresponding to metallic copper (Cu) and nickel (Ni) in the XPS analysis is entirely expected. Therefore, the results from the XPS measurements indicate the presence of approximately 3 nanometers of

copper oxide and nickel oxide on the surfaces of the copper and nickel nanoparticles but should not be misinterpreted as a definitive absence of metallic copper and nickel on the surface of the μ -Al substrate. Moreover, the X-Ray diffraction (XRD) pattern revealed no discernible diffraction peaks corresponding to copper oxide or nickel oxide; instead, only the distinct peaks of elemental copper and elemental nickel were observed. This finding suggests that the oxidation levels of the copper and nickel metals are not sufficiently pronounced to be detected by XRD analysis. It is important to acknowledge that, in the context of the thermolysis of ammonium perchlorate, the catalytic efficacy of nano-sized copper (nCu) and nano-sized nickel (nNi) is fundamentally comparable to that of their oxide counterparts, nCuO and nNiO [44,45]. Nonetheless, as we progress with material synthesis, it remains imperative to address the oxidation susceptibility of metallic copper and nickel in future investigations. In summary, this study confirms the presence of elemental nickel and elemental copper through XRD and VSM tests, indicating that the synthesis of (nCu+nNi)/ μ Al composite particles has been successful. The principal challenge now is to devise strategies to mitigate excessive oxidation of metallic nCu and nNi during the preparation process.

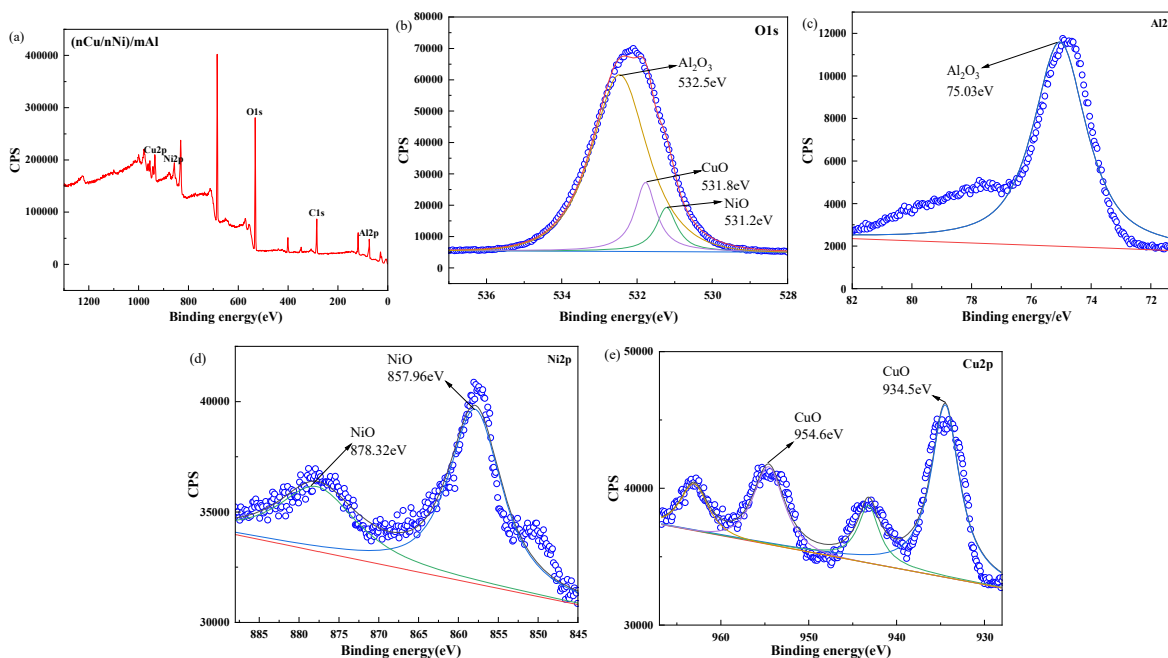


Figure 3. XPS spectra of [nCu+nNi]/ μ Al and [nCu+nNi] shell: (a) whole spectrum; (b) for O1s; (c) for Al2o; (d) for Ni2p; (e) for Cu2p.

Figure 4 presents the laser confocal microscopy scanning image of (nCu+nNi)/ μ Al composite microspheres. Panel 64 exhibits a two-dimensional pseudocolor map of a randomly selected composite microsphere, wherein a circular distribution of colors signifies varying distances from each position on the microsphere to the reference plane [46]. These findings illustrate that the microspheres exhibit commendable sphericity. Observed from the top view in Figure 4c, the contour lines representing the surface roughness of the microspheres reveal a relatively smooth surface [47]. This indicates that the nano-Cu and nano-Ni effectively create a cohesive coating on the μ Al particle surfaces, demonstrating a highly proficient coating quality.

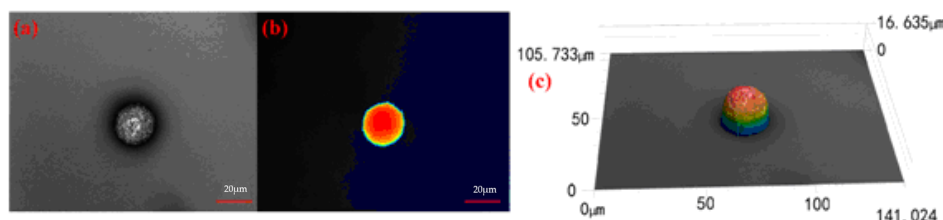


Figure 4. Laser microscope photos of $[n\text{Cu}+n\text{Ni}]/\mu\text{Al}$ microspheres: (a) color of $[n\text{Cu}+n\text{Ni}]/\mu\text{Al}$; (b) height of $[n\text{Cu}+n\text{Ni}]/\mu\text{Al}$; (c) 3D image of $[n\text{Cu}+n\text{Ni}]/\mu\text{Al}$.

2.2. Thermal Analyses

In this study, we aim to investigate the benefits of surface coating with nano-copper ($n\text{Cu}$) and nano-nickel ($n\text{Ni}$) as alternatives to alumina, specifically to enhance the oxidation activity of micron-sized aluminum (μAl) and to facilitate the dispersion of nano-catalysts for the thermolysis of ammonium perchlorate. To achieve this, we conducted a series of thermal analysis tests on the samples. Initially, thermogravimetric-differential scanning calorimetry (TG-DSC) was performed on the $[n\text{Cu}+n\text{Ni}]/\mu\text{Al}$ composite in an oxygen-rich environment, allowing for a comparative analysis with unmodified μAl . The findings are illustrated in Figure 5. In Figure 5a, the DSC, TG, and derivative thermogravimetric (DTG) curves of unaltered μAl are presented. The DSC curve distinctly reveals a pronounced endothermic peak at approximately 660 degrees Celsius, indicative of the melting phase of μAl . Concurrently, a broad exothermic peak emerges around 1200 degrees Celsius, which can be attributed to the oxidation of μAl by atmospheric oxygen. The TG curve indicates that the weight gain of pristine μAl in the presence of oxygen reaches approximately 105% at 1200 °C, a finding that corroborates previous studies conducted by other scholars [12]. In contrast, the weight gain of the $[n\text{Cu}+n\text{Ni}]/\mu\text{Al}$ composite attains around 120% at a notably lower temperature of 950 °C, aligning closely with theoretical predictions. Notably, as illustrated in Figure 5b, the DSC curve for $[n\text{Cu}+n\text{Ni}]/\mu\text{Al}$ reveals an exothermic peak attributed to its reaction with oxygen at approximately 880 °C. In comparison, the DSC peak for μAl occurs around 1200 °C. These observations suggest that the oxidation process of $[n\text{Cu}+n\text{Ni}]/\mu\text{Al}$ occurs to a significantly greater extent than that of pristine μAl in an oxygen environment. The potential mechanisms by which nanoscale metallic particles augment the thermal reactivity of μAl were thoroughly elucidated in the introduction [29,30].

Next, we shall examine the catalytic effects of the $[n\text{Cu}+n\text{Ni}]/\mu\text{Al}$ composite on the thermal decomposition of ammonium perchlorate. Initially, we employed a physical mixing technique to combine a specified quantity of raw μAl with raw AP. Subsequently, $[n\text{Cu}+n\text{Ni}]/\mu\text{Al}$ was blended with the raw AP, adhering to the stoichiometric ratio delineated in Equation 1 for the mass ratio of μAl (or $[n\text{Cu}+n\text{Ni}]/\mu\text{Al}$) to raw AP. For clarity, we designate the two resultant mixtures as $(\mu\text{Al}+\text{AP})$ and $([n\text{Cu}+n\text{Ni}]/\mu\text{Al}+\text{AP})$. DSC analyses were performed on these mixtures as well as on pure AP, and the findings are illustrated in Figure 6. As depicted in Figure 6a, the DSC curve for $(\mu\text{Al}+\text{AP})$ reveals a minor endothermic peak coupled with a prominent exothermic peak, corresponding to the crystal transformation of AP and its subsequent thermal decomposition, respectively. Furthermore, with an increase in the heating rate, the temperature corresponding to the phase transition peak of AP remained relatively unchanged, whereas the temperature of the decomposition peak exhibited a notable increase. The DSC traces of pure AP at various heating rates are illustrated in Figure 6c. These traces demonstrate that pure AP consistently displays a crystalline transformation peak in addition to a thermolysis peak. Notably, the temperatures of both the crystalline transformation peak and the thermolysis peak correspond closely to those observed in the $[\mu\text{Al}+\text{AP}]$ samples. This observation suggests that the incorporation of μAl does not significantly modify the thermal decomposition profile of AP, indicating

that pure μ Al has negligible catalytic influence on the thermal decomposition of AP. In Figure 6b, for the AP composite doped with [nCu+nNi]/ μ Al, there was no significant alteration in the crystalline transformation peak; however, the temperature of its thermal decomposition peak demonstrated a marked decrease in comparison to the values depicted in Figure 6a,c. In Figure 6b, the DSC curve for the composite [nCu+nNi]/ μ Al+AP, recorded at a heating rate of $15\text{ }^{\circ}\text{C}/\text{min}$, reveals a pronounced exothermic peak at $336.3\text{ }^{\circ}\text{C}$, indicative of the thermal decomposition of catalyzed AP. In contrast, the exothermic peaks for pure AP and the combination (μ Al+AP) occur at higher temperatures, specifically at $430.4\text{ }^{\circ}\text{C}$ and $434.4\text{ }^{\circ}\text{C}$, respectively. This observation underscores the potent catalytic effects exerted by nCu and nNi when adsorbed onto the surface of μ Al, as their incorporation markedly accelerates the thermal decomposition of AP. Such a finding is indeed an encouraging indication of enhanced reactivity.

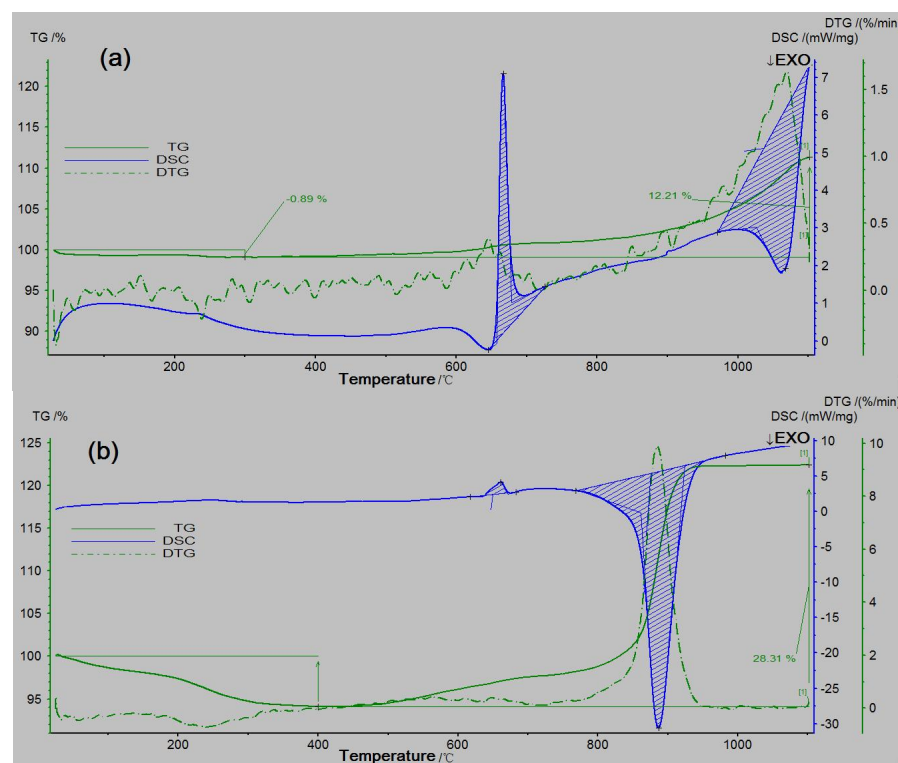


Figure 5. TG–DSC curves of raw μ Al (a) and [nCu+nNi]/ μ Al (b).



It is well acknowledged that the limited dispersibility of nanoparticles within the system has long posed a formidable challenge in this field. In this study, we initially applied a combined coating of nano-copper and nano-nickel onto the surface of μ Al and subsequently blended this composite with pure AP. This novel approach markedly enhances the dispersibility of the nanoparticles, constituting a significant technological advancement relative to prior research. The [nCu+nNi]/ μ Al composite material has good dispersibility, which improves its activity; on the other hand, the Cu and Ni metal particles used have high activity and act as nanocatalysts in the reaction, which improves the reactivity of nano-aluminum powder. Table 1 shows that at the heating rate of $5\text{ }^{\circ}\text{C}/\text{min}$, the exothermic peak of AP has different degrees of change under different modification methods. However, after adding [nCu+nNi]/ μ Al, compared with the raw AP, the exothermic decomposition peak of the modified AP was advanced by the most, reaching $99.3\text{ }^{\circ}\text{C}$. The exothermic peaks of $20\text{ }^{\circ}\text{C}/\text{min}$ doped with nano-copper and nano-nickel are $367\text{ }^{\circ}\text{C}$ and $388\text{ }^{\circ}\text{C}$, respectively, which were $110.2\text{ }^{\circ}\text{C}$ and $89.2\text{ }^{\circ}\text{C}$ earlier, respectively. But this is achieved at a heating rate of

20 °C/min. It is evident that the catalytic efficacy of the [nCu+nNi] composite significantly surpasses that of the individual catalysts, nCu or nNi. This underscores the phenomenon of catalytic synergy.

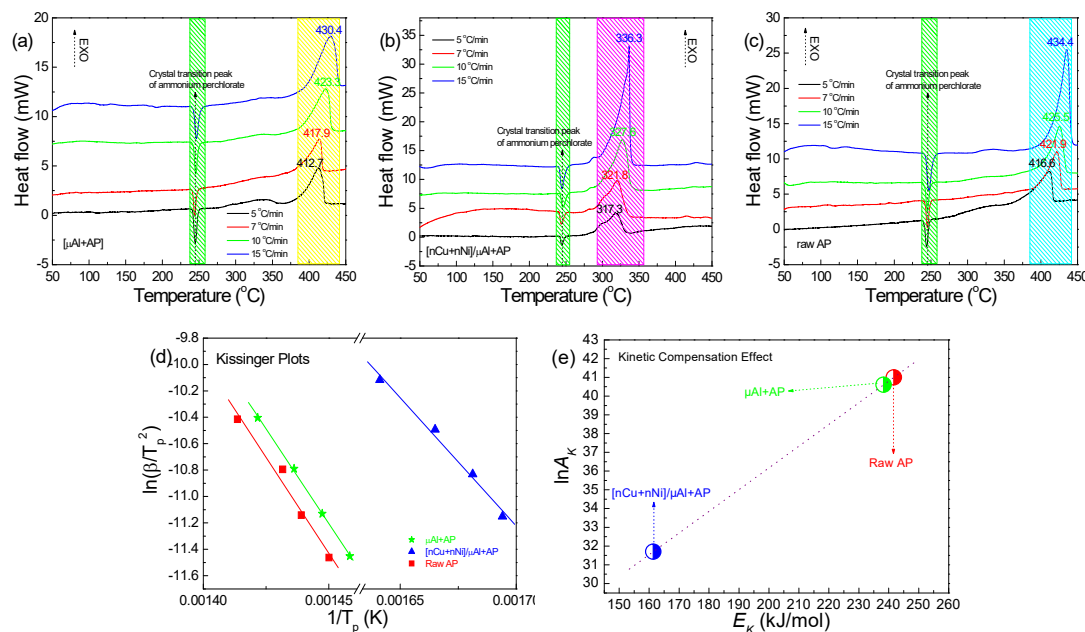


Figure 6. DSC traces of samples: (a) $\mu\text{Al}+\text{AP}$; (b) $[\text{nCu}+\text{nNi}]/\mu\text{Al}+\text{AP}$; (c) raw AP; (d) fitting curves; (e) fit degree.

Table 1. Peak temperature of AP under different modification methods.

Sample	Modification Method	Original Peak Temperature/°C	Modified Peak Temperature/°C	Advance Temperature/°C
Ultra-fine AP [48]	Microfluidics	390.2	377.94	12.26
Cu+AP [23]	Directly doping	477.2	367	110.2
Ni+AP [23]	Directly doping	477.2	388	89.2
AP@Al [49]	Surface coating	399.44	387.31	12.13
$\mu\text{Al}+\text{AP}$	Directly doping	416.6	412.7	3.9
$[\text{nCu}+\text{nNi}]/\mu\text{Al}+\text{AP}$	Directly doping	416.6	317.3	99.3

The various thermochemical parameters were computed using Equations (2)–(6) [50], allowing for the characterization of the thermodynamic and kinetic properties of raw ammonium perchlorate and AP doped with μAl or a combination of $[\text{nCu}+\text{nNi}]/\mu\text{Al}$. The findings are presented in Figure 6d and summarized in Table 2. Notably, Figure 6d illustrates that the relationship between $1/T_p$ and $\ln(\beta/T_p^2)$ for all samples demonstrates a robust linear correlation, with a coefficient of determination (R^2) exceeding 0.99. This suggests that the activation energy and pre-exponential factor derived from DSC data are highly precise. The kinetic data in Table 1 reveal that the activation energy (E_K) for all reactions ranges from 161 to 242 kJ/mol, with the E_K value for $[\text{nCu}+\text{nNi}]/\mu\text{Al}+\text{AP}$ being lower than that of both raw AP and $\mu\text{Al}+\text{AP}$ [51–53]. However, the rate constants (k) for the three samples do not exhibit significant disparities. Thermodynamic analysis reveals that the activation enthalpy (ΔH^\ddagger) for the composite $[\text{nCu}+\text{nNi}]/\mu\text{Al}+\text{AP}$ approaches its minimum

value, signifying that its activation process necessitates the absorption of comparatively less heat. Notably, the activation enthalpy for $[n\text{Cu}+n\text{Ni}]/\mu\text{Al+AP}$ is demonstrably lower than that of the other samples. The variations in activation free energy (ΔG^\neq) among the three samples are minimal, and all values are positive, indicating that the activation processes for both raw AP and catalyzed AP are non-spontaneous, necessitating the absorption of a specific amount of heat to attain the activated state. All recorded values of activation entropy (ΔS^\neq) are positive, suggesting an increase in the degree of freedom within the systems following activation and indicating the potential generation of gas during the activation process. The kinetic compensation effect illustrated in Figure 6e reveals that the $[E_K - \ln(A_K)]$ data points for the three exothermic reactions align in a linear fashion, signifying a uniformity in their kinetic mechanisms concerning thermal reactions. This consistency is understandable, as each exothermic peak is associated with the thermal decomposition of ammonium perchlorate.

$$\ln \frac{\beta}{T_p^2} = \ln \frac{R \cdot A_K}{E_K} - \frac{E_K}{R} \cdot \frac{1}{T_p} \quad (2)$$

$$k = A_K \cdot \exp\left(-\frac{E_K}{T_p \cdot R}\right) \quad (3)$$

$$A \exp\left(-\frac{E_K}{RT_P}\right) = \frac{K_B T_P}{h} \exp\left(-\frac{\Delta G^\neq}{RT_P}\right) \quad (4)$$

$$\Delta H^\neq = E_K - RT_P \quad (5)$$

$$\Delta G^\neq = \Delta H^\neq - T_P \Delta S^\neq \quad (6)$$

where T_p is the peak temperature in the DSC trace with a heating rate of $10\text{ }^\circ\text{C min}^{-1}$; K_B and h are the Boltzmann ($K_B = 1.381 \times 10^{-23}\text{ J/K}$) and Planck constants ($h = 6.626 \times 10^{-34}\text{ J/s}$), respectively; β is the heating rate; T_{ei} is the extrapolated onset temperature at a specific heating rate; T_{eo} is the extrapolated onset temperature at the heating rate closest to zero; Q is the theoretical decomposition heat per mole of explosive; M is the theoretical mass per mole of explosive; E_K and A_K are the activation energy and pre-exponential factor calculated by the Kissinger equation.

Table 2. Data of thermodynamics, kinetics, and 5-s burst points.

Samples	$T_p\text{ (}^\circ\text{C)}$ ($10\text{ }^\circ\text{C/min}$)	Thermodynamic			Kinetics		Burst Points		
		ΔH^\neq (kJ/mol)	ΔG^\neq (kJ/mol)	ΔS^\neq (J/mol·K)	E_K (kJ/mol)	$\ln A_K$	k (s $^{-1}$)	T_{5s} ($^\circ\text{C}$)	E (kJ/mol)
Raw AP	425.5	235.8	179.6	0.08	241.7	41.0	0.54	288	28.4
$\mu\text{Al+AP}$	423.3	232.5	178.6	0.08	238.3	40.6	0.59	284	44.2
$[n\text{Cu}+n\text{Ni}]/\mu\text{Al+AP}$	327.6	156.4	153.9	0.04	161.4	31.7	0.52	302	35.4

In order to investigate the catalytic mechanism of $[n\text{Cu}+n\text{Ni}]/\mu\text{Al}$ on the thermal decomposition of AP, we conducted TG-IR-MS combined analysis on $[n\text{Cu}+n\text{Ni}]/\mu\text{Al+AP}$ samples, and the results are shown in Figure 7. Figure 7 predominantly involved the thermal decomposition of the ammonium perchlorate without substantial reaction with μAl . The thermal decomposition profile of $[n\text{Cu}+n\text{Ni}]/\mu\text{Al+AP}$ reveals that its initiation temperature is approximately 300 degrees Celsius, with its thermal decomposition occurring significantly earlier than that of the two other samples. This observation underscores the considerable catalytic influence exerted by the nCu and nNi coatings on the surface of μAl during the thermal decomposition of ammonium perchlorate. In contrast, pure

aluminum exhibits no catalytic effect on this decomposition process. Furthermore, post-decomposition analysis indicates that approximately 28 wt.% of residual mass remains, suggesting that the residual material comprises $[n\text{Cu}+n\text{Ni}]/\mu\text{Al}$. This finding is largely consistent with the designed mass ratio of $[n\text{Cu}+n\text{Ni}]/\mu\text{Al}$ to ammonium perchlorate. This observation suggests that throughout the heating process, no thermal reaction occurred between $[n\text{Cu}+n\text{Ni}]/\mu\text{Al}$ and AP. Instead, $[n\text{Cu}+n\text{Ni}]/\mu\text{Al}$ served solely as a catalyst for the thermal decomposition of AP, thereby significantly enhancing the rate of this decomposition. The DTG curves presented in Figure 7b further illustrate that the decomposition profiles of $\mu\text{Al}+\text{AP}$ and raw AP are fundamentally analogous. In contrast, the thermal decomposition of $[n\text{Cu}+n\text{Ni}]/\mu\text{Al}+\text{AP}$ is markedly advanced. Additionally, the DTG peak associated with $[n\text{Cu}+n\text{Ni}]/\mu\text{Al}+\text{AP}$ is considerably more pronounced than those corresponding to $\mu\text{Al}+\text{AP}$ and raw AP, indicating a significantly elevated thermal weight loss rate for $[n\text{Cu}+n\text{Ni}]/\mu\text{Al}+\text{AP}$ relative to its counterparts. This finding underscores the potent catalytic influence of $[n\text{Cu}+n\text{Ni}]/\mu\text{Al}$ on the thermal decomposition of AP while simultaneously suggesting an absence of reaction between $[n\text{Cu}+n\text{Ni}]/\mu\text{Al}$ and either AP or its thermal decomposition products at lower temperatures. In addition, Figure 7c,d jointly demonstrate that after the addition of $[n\text{Cu}+n\text{Ni}]/\mu\text{Al}$, the thermal decomposition of AP generates a large amount of H_2O , a certain amount of HCl , N_2O , O_2 , and a small amount of NO. The generation of O_2 indicates that the thermal decomposition products of AP have not reacted with $[n\text{Cu}+n\text{Ni}]/\mu\text{Al}$, which is caused by insufficient temperature, as the oxidation of $[n\text{Cu}+n\text{Ni}]/\mu\text{Al}$ occurs at least above 800 degrees Celsius. The impurity in the CO_2 peak data in Figure 7c comes from the decomposition of a small amount of CO_2 and organic matter in the air, which is a normal phenomenon. Compared with the TG-IR spectra of pure AP in reference [38], it can be seen that overall, within 500 degrees Celsius, the thermal decomposition mechanism of $[n\text{Cu}+n\text{Ni}]/\mu\text{Al}+\text{AP}$ is basically the same as that of pure AP.

The thermal sensitivity of energetic materials is intrinsically linked to their thermal decomposition characteristics. In this study, we examined the thermal sensitivities of raw AP, μAl combined with AP, and a composite of $[n\text{Cu}+n\text{Ni}]/\mu\text{Al}$ mixed with AP, as assessed through burst point experiments. The findings are presented in Table 1 and illustrated in Figure 8. The methodologies employed for determining the 5-s burst point (T_{5s}) and the activation energy (E) are detailed in references [54–56]. Furthermore, in the burst point experiments, the mass ratio of μAl (or $[n\text{Cu}+n\text{Ni}]/\mu\text{Al}$) to raw AP adheres to the stoichiometric ratios delineated in Equation (1). The results indicate that the T_{5s} of the three samples consistently range from 284 to 302 °C, revealing no significant discrepancies among the samples. Notably, the larger sample size employed in the burst point tests, in contrast to that used in DSC experiments, resulted in the observed 5-s burst points being significantly lower than the exothermic peak temperatures recorded in the DSC analyses. This observation constitutes a standard experimental phenomenon. In the analysis of the three samples discussed in this article, the explosion points displayed no significant differences, indicating that the thermal sensitivity of ammonium perchlorate remains largely unaffected by the surface coating of μAl . The variation in activation energy (E) exhibited a pattern consistent with alterations in T_{5s} . The activation energies for the samples were found to lie within the range of 28~45 kJ/mol, with only minor fluctuations. As illustrated in Figure 8c, there is no discernible linear relationship between T_{5s} and E across all samples, suggesting that the kinetic mechanisms governing the reactions of these samples diverge significantly. In summary, the thermal sensitivity of AP doped with the $[n\text{Cu}+n\text{Ni}]/\mu\text{Al}$ composite is comparable to that of both raw AP and AP doped solely with μAl . This observation indicates that the incorporation of the $[n\text{Cu}+n\text{Ni}]/\mu\text{Al}$ composite does not enhance the thermal sensitivity of ammonium perchlorate.

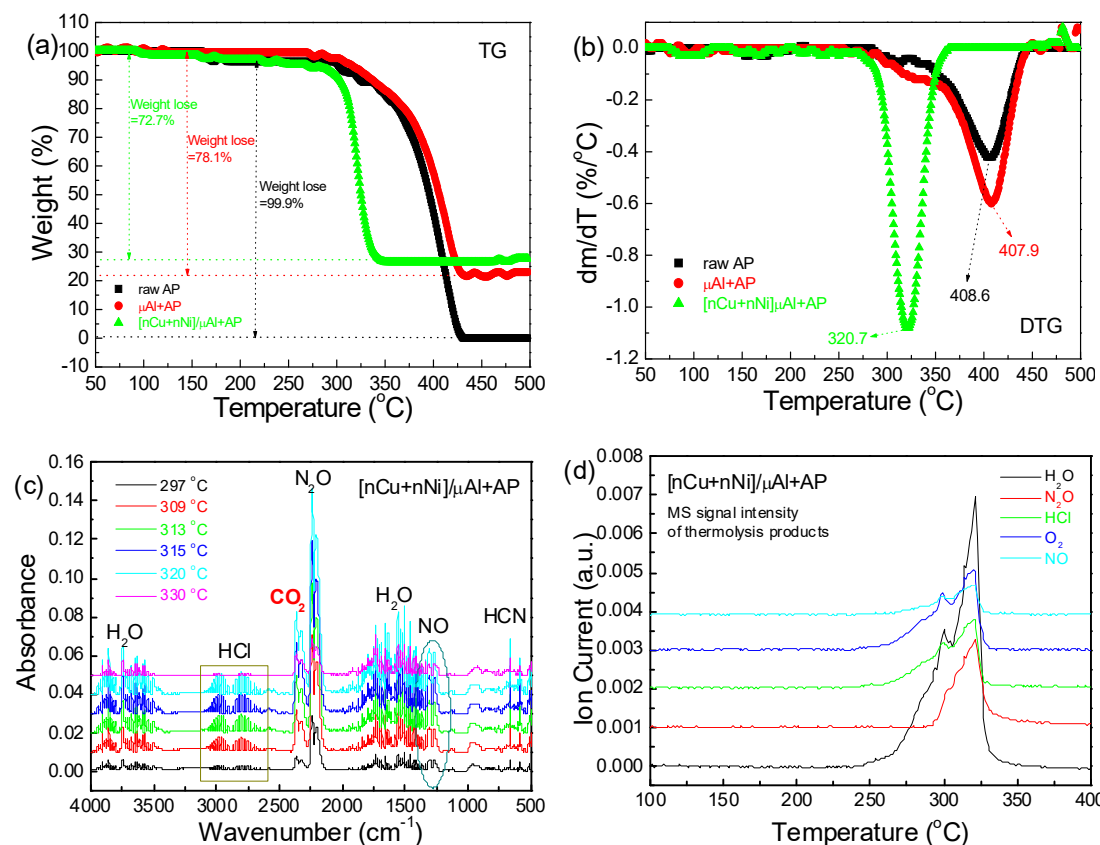


Figure 7. TG–IR–MS combined analyses of samples: (a) TG traces; (b) DTG curves; (c) IR spectra of thermolysis products of $[\text{nCu}+\text{nNi}]/\mu\text{Al}+\text{AP}$; (d) MS signal intensity of thermolysis products of $[\text{nCu}+\text{nNi}]/\mu\text{Al}+\text{AP}$.

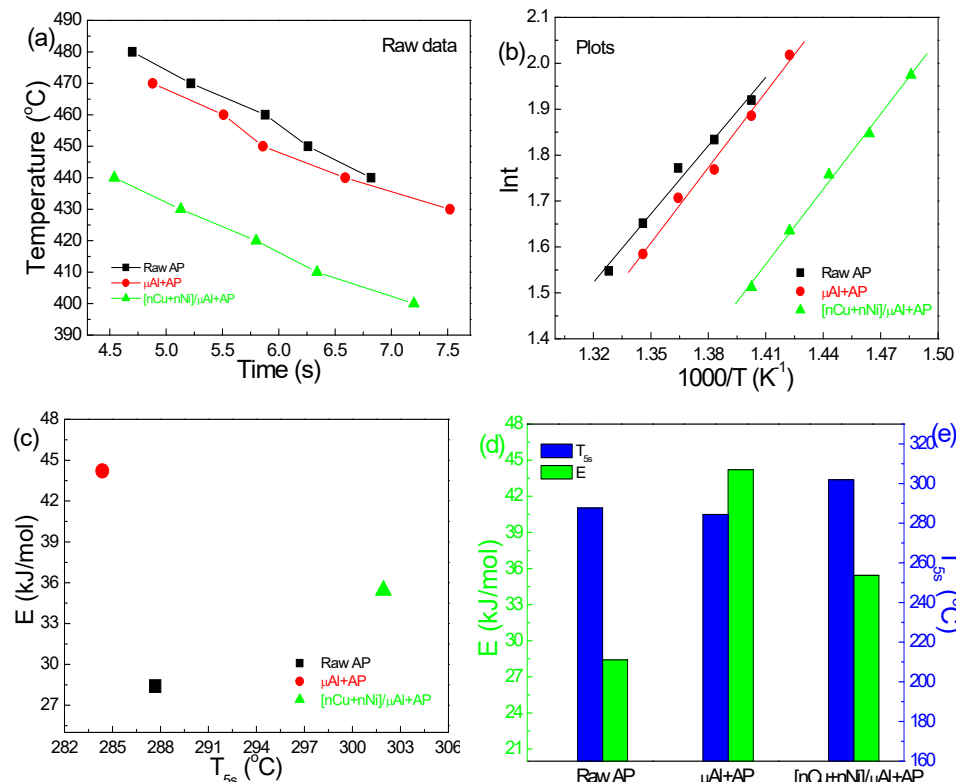


Figure 8. Burst point testing of samples: (a) the raw data; (b) the plots; (c) $E-T_{5s}$; (d) the histograms.

2.3. Combustion Performance

2.3.1. Combustion in Closed Bomb

To conduct a preliminary investigation into the influence of $[n\text{Cu}+n\text{Ni}]$ on the combustion performance of μAl and ammonium perchlorate, we meticulously introduced a measured quantity of the sample into a sealed combustion bomb and initiated ignition using a heated wire. A pressure sensor was repurposed to monitor and document the fluctuations in pressure within the confined explosive chamber over time, while a high-speed camera captured the combustion flame dynamics of the sample. The results are presented in Figure 9. For the various combinations of fuel and oxidizer, the mass ratio of the fuel (μAl or $[n\text{Cu}+n\text{Ni}]/\mu\text{Al}$) to the oxidizer (AP) aligns with the zero-oxygen equilibrium stoichiometric ratio outlined in Equation (1). Observations in Figure 9a and Figure 11 reveal that both the raw AP and the μAl +AP mixture exhibit minimal combustion under the hot wire ignition conditions, resulting in only a faint flame, which primarily corresponds to their thermal decomposition. However, Figure 9c illustrates that the mixture of $[n\text{Cu}+n\text{Ni}]/\mu\text{Al}$ +AP experienced vigorous combustion under identical conditions. Notably, within the interval of 499 to 982 milliseconds, the high-speed camera captured exceptionally luminous flames. Figure 9d,e reveals that the pressure variations resulting from the combustion or decomposition of both raw AP and μAl +AP are negligible. In contrast, Figure 9f,g demonstrates that the combustion of $[n\text{Cu}+n\text{Ni}]/\mu\text{Al}$ +AP induces a substantial increase in pressure within the sealed explosive apparatus. Furthermore, the rate of pressure augmentation associated with the combustion of $[n\text{Cu}+n\text{Ni}]/\mu\text{Al}$ +AP significantly surpasses that observed for raw AP and μAl +AP. Consequently, the combustion experiment conducted in a sealed explosive apparatus demonstrated that the $[n\text{Cu}+n\text{Ni}]$ coating on the surface of micro-aluminum markedly enhanced the combustion performance of ammonium perchlorate and μAl . In this context, both AP and μAl exhibited vigorous combustion under sealed conditions. Conversely, the unrefined AP and the mixture of μAl with AP exhibited negligible ignition.

2.3.2. Combustion in the Air

In addition to the investigations of constant-volume combustion within a sealed explosive device, we also examined the combustion characteristics of three samples in an atmospheric environment at room temperature and pressure, as illustrated in Figure 10. The specific fuel and oxidizer combinations were selected such that the mass ratio of the fuel—represented by either μAl or the equivalent proportion of $[n\text{Cu}+n\text{Ni}]/\mu\text{Al}$ —to the oxidizer (AP) correlates with the zero-oxygen equilibrium stoichiometric ratio outlined in Equation (1). During this assessment, we observed that neither raw AP nor μAl could be ignited by the hot wire. Consequently, the infrared camera failed to register any flame indicative of their combustion, precluding the possibility of measuring combustion temperatures via flame analysis. In contrast, the composition of $[n\text{Cu}+n\text{Ni}]/\mu\text{Al}$ +AP exhibited vigorous combustion when subjected to ignition via the hot wire. The thermal infrared images presented in Figure 10a–f illustrate that the combustion of the $[n\text{Cu}+n\text{Ni}]/\mu\text{Al}$ +AP composite occurs in two distinct processes, which engender two vibrant flames. The temperature-time curve depicted in Figure 10g further corroborates this observation. Infrared camera measurements reveal that the peak temperatures recorded during the combustion of $[n\text{Cu}+n\text{Ni}]/\mu\text{Al}$ +AP are merely 1851 °C and 1753 °C, considerably lower than the theoretically predicted value of 3389 °C (refer to Table 3). This discrepancy is attributed to incomplete combustion of the $[n\text{Cu}+n\text{Ni}]/\mu\text{Al}$ +AP mixture and does not reflect any inaccuracies in the theoretical or experimental data; indeed, both sets of values remain valid. Furthermore, the thermal infrared camera findings unequivocally demonstrate that the combustion performance of $[n\text{Cu}+n\text{Ni}]/\mu\text{Al}$ +AP is markedly superior to that of raw

ammonium perchlorate and the $\mu\text{Al}+\text{AP}$ mixture. This reinforces the assertion that the $[\text{nCu}+\text{nNi}]$ compound significantly enhances the combustion efficiency of micro-aluminum in conjunction with AP.

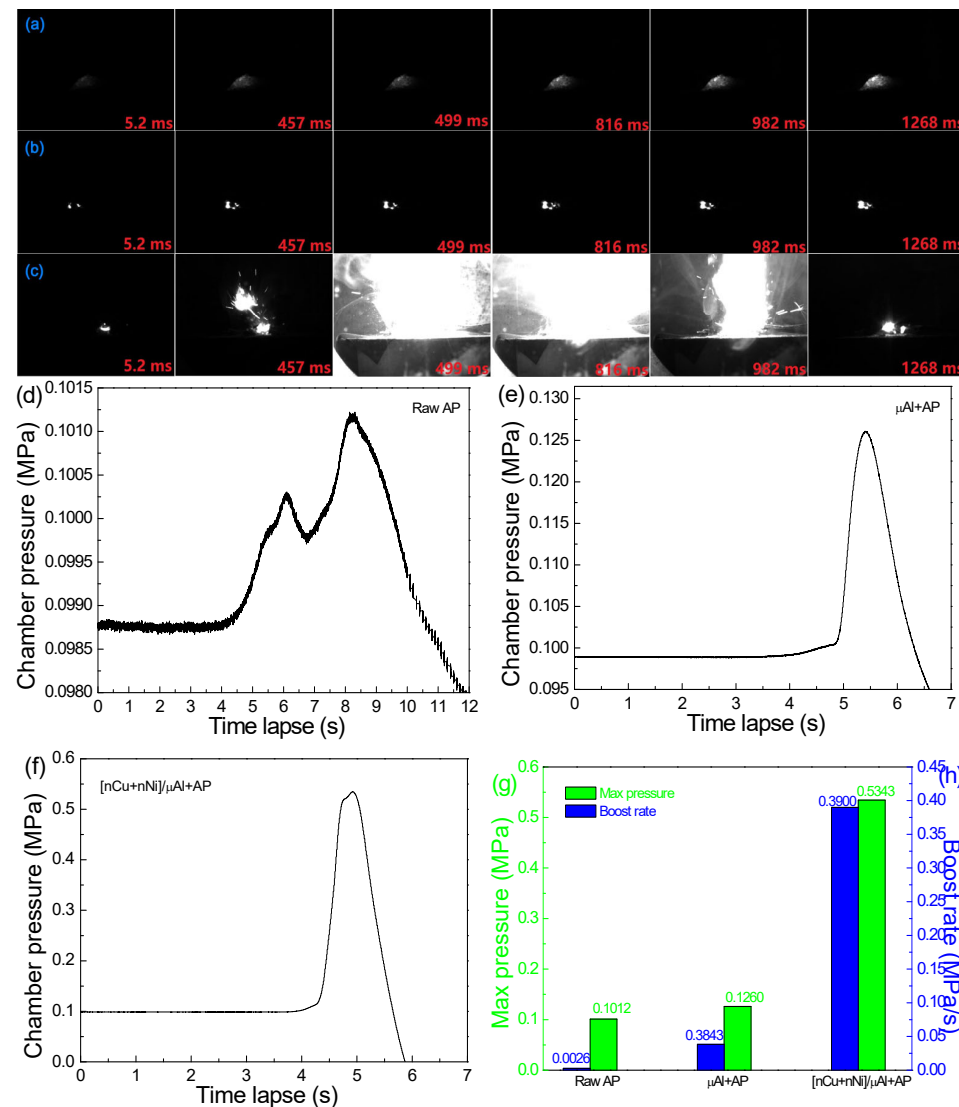


Figure 9. Combustion performance of samples: (a) flame images of raw AP; (b) flame images of $\mu\text{Al}+\text{AP}$; (c) flame images of $[\text{nCu}+\text{Ni}]/\mu\text{Al}+\text{AP}$; (d) pressure curve of raw AP; (e) pressure curve of $\mu\text{Al}+\text{AP}$; (f) pressure curve of $[\text{nCu}+\text{Ni}]/\mu\text{Al}+\text{AP}$; (g) max pressures and boost rates.

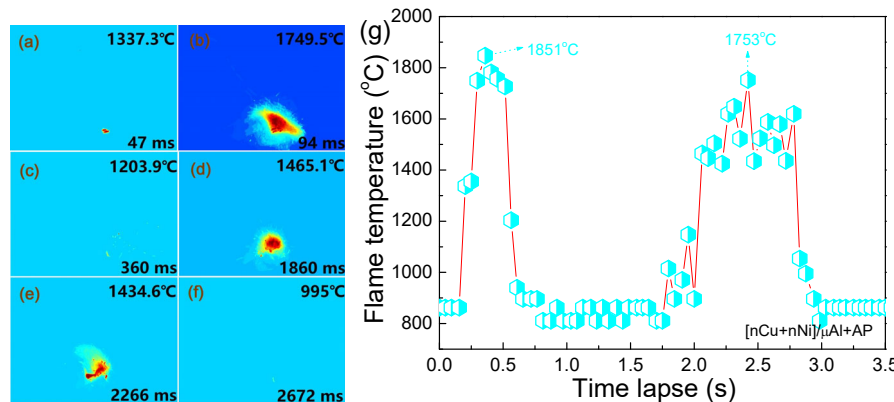


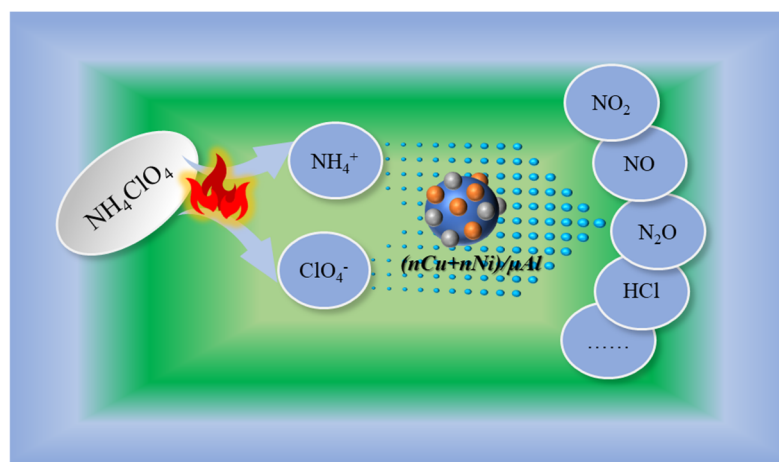
Figure 10. Thermal infrared images (a-f) and curves of burning time to flame temperature (g) of $[\text{nCu}+\text{Ni}]/\mu\text{Al}+\text{AP}$.

Table 3. Thermodynamic data of combustion of samples at atmospheric pressure.

Samples	$T_{TOP,exp}$ (°C)	$T_{ad,cal}$ (°C)	$H_{R,cal}$ (kJ/kg)	$H_{P,cal}$ (kJ/kg)	$\Delta H_{C,cal}$ (kJ/kg)
Raw AP	-	1376	-2520	-4852	-2332
$\mu\text{Al}+\text{AP}$	-	3420	-1822	-11,968	-10,146
$[\text{nCu+nNi}]/\mu\text{Al}+\text{AP}$	1851	3389	-1823	-11,647	-9824

Note: In Table 3, $T_{TOP,exp}$ are the highest flame temperatures measured from the combustion of the sample at $P_C = 1$ atm; $T_{ad,cal}$ is the adiabatic flame temperature calculated using NASA-CEA2 at $P_C = 1$ atm and $\Delta H = 0$ kJ/kg; $H_{R,cal}$ is the total enthalpy of the sample before combustion calculated using NASA-CEA2 at $P_C = 1$ atm and $T_0 = 298$ K; $H_{P,cal}$ is the total enthalpy of combustion products of the sample calculated using NASA-CEA2 at $P_C = 1$ atm and $T_0 = 298$ K; $\Delta H_{C,cal}$ is the enthalpy change (total heat release) of the sample during combustion calculated using NASA-CEA2 at $P_C = 1$ atm and $T_0 = 298$ K.

Consequently, whether in a sealed bomb or ambient air, the incorporation of nano-sized copper and nickel significantly enhances the combustion efficiency of ammonium perchlorate at an initial pressure of 1 atm and a temperature of 298 K. Current technological limitations hinder our comprehensive understanding of the catalytic mechanisms by which nano-copper (nCu) and nano-nickel (nNi) facilitate the thermal decomposition and combustion of ammonium perchlorate. However, it can be firmly established that at lower temperatures, nano-copper and nano-nickel engage in redox reactions with oxidants prior to the involvement of metallic aluminum within an oxidative environment, resulting in the formation of corresponding copper oxide and nickel oxide. These oxidation-reduction processes proceed with remarkable rapidity and intensity, releasing substantial quantities of heat, thereby acting as numerous nano-scale active centers throughout the thermal decomposition or combustion of ammonium perchlorate. Indeed, the catalytic influence of $[\text{nCu+nNi}]$ on the combustion of $\text{AP}+\mu\text{Al}$ is markedly superior to their catalytic impact on the thermal decomposition of AP. As illustrated in Figure 11, throughout the combustion process of $[\text{nCu+nNi}]/\mu\text{Al}+\text{AP}$, $[\text{nCu+nNi}]$ not only facilitates the thermal decomposition of AP but also enhances the oxidation reaction of μAl , which is typically inhibited by the presence of the oxide layer. Thus, based on the inferred combustion mechanism and the empirical data, it becomes evident that under the dual influence of $[\text{nCu+nNi}]$, the system $[\text{nCu+nNi}]/\mu\text{Al}+\text{AP}$ demonstrates exceptional combustion performance.

**Figure 11.** Speculation diagram of catalysis mechanism of coated Al.

The combustion process of three distinct samples at a pressure of 1 atm was meticulously simulated using the NASA-CEA2 code, and a variety of parameters were subsequently calculated. The findings are presented in Table 3 and illustrated in Figure 12. It is evident from Table 3 that the adiabatic flame temperature predicted by the NASA-

CEA2 model is lower than the experimentally measured flame temperature. The computational results indicate that the adiabatic flame temperatures for the $\mu\text{Al+AP}$ and $[\text{nCu+nNi}]/\mu\text{Al+AP}$ formulations are comparably elevated, significantly surpassing the adiabatic flame temperature of pure ammonium perchlorate. From a theoretical standpoint, it can be inferred that the adiabatic flame temperature of $\mu\text{Al+AP}$ marginally exceeds that of $[\text{nCu+nNi}]/\mu\text{Al+AP}$, attributable to the considerably lower combustion heat released by copper and nickel in contrast to aluminum. Nevertheless, an analysis of the experimental results indicates that $\mu\text{Al+AP}$ did not experience significant combustion; rather, it underwent thermal decomposition. In contrast, the mixture of $[\text{nCu+nNi}]/\mu\text{Al+AP}$ displayed vigorous combustion, culminating in a considerably elevated combustion temperature. Despite both $\mu\text{Al+AP}$ and $[\text{nCu+nNi}]/\mu\text{Al+AP}$ exhibiting a negative change in free energy from a thermodynamic perspective, notable discrepancies emerge in the kinetics of their combustion reactions under equivalent hot wire ignition conditions. The combustion reaction rate for $[\text{nCu+nNi}]/\mu\text{Al+AP}$ is markedly superior to that of $\mu\text{Al+AP}$. Consequently, although $\mu\text{Al+AP}$ is represented in Table 3 as having greater heat release and a higher adiabatic flame temperature, its practical combustion performance remains inadequate, characterized solely by thermal decomposition rather than vigorous combustion phenomena. This finding further substantiates that the combined presence of $[\text{nCu+nNi}]$ exerts a pronounced catalytic influence on the combustion kinetics of AP and μAl . As depicted in Figure 12, there exists a remarkable consistency between the predicted combustion products and their corresponding mole fractions, specifically $\mu\text{Al+AP}$ and $[\text{nCu+nNi}]/\mu\text{Al+AP}$. The resultant combustion products are characterized by a substantial presence of chlorine (Cl), hydrogen (H), hydrogen chloride (HCl), dihydrogen (H₂), water (H₂O), nitrogen (N₂), oxygen (O₂), and solid aluminum oxide (Al₂O₃). Notably, this observation suggests that, despite the stoichiometric ratio indicating a zero oxygen equilibrium, the predicted products remain oxygen-rich. This finding implies, to a certain extent, that formulations exhibiting a marginally negative oxygen balance are associated with optimal reaction performance, characterized by the highest combustion heat and adiabatic flame temperature.

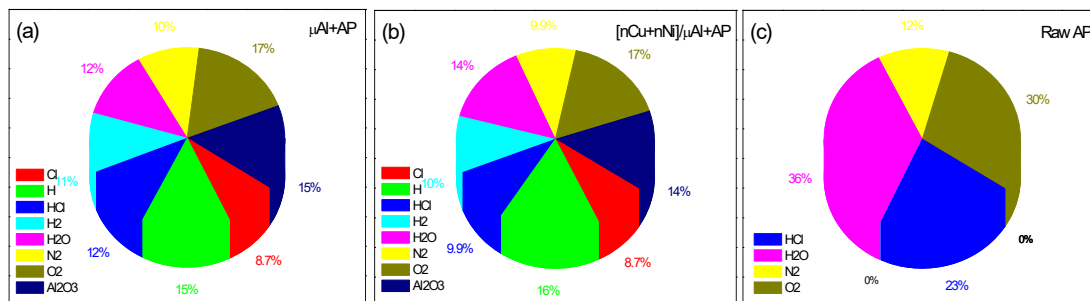


Figure 12. The molar ratio of combustion products of samples: (a) $\mu\text{Al+AP}$; (b) $[\text{nCu+nNi}]/\mu\text{Al+AP}$; (c) Raw AP.

2.3.3. Heats of Combustion in Oxygen Bomb

In this study, we employed an automatic calorimeter to quantify the heat of combustion for four distinct samples under pressure of 3 MPa in pure oxygen: raw μAl , $[\text{nCu+nNi}]/\mu\text{Al}$, $\mu\text{Al+AP}$, and $[\text{nCu+nNi}]/\mu\text{Al+AP}$. The results of these tests are illustrated in Figure 13. For both $\mu\text{Al+AP}$ and $[\text{nCu+nNi}]/\mu\text{Al+AP}$, the mass ratio of μAl or $[\text{nCu+nNi}]/\mu\text{Al}$ to ammonium perchlorate corresponds to the zero oxygen equilibrium stoichiometric ratio as defined in Equation (1). It is noteworthy that, during this experiment, the combustion of raw μAl and $[\text{nCu+nNi}]/\mu\text{Al}$ in an oxygen environment exhibited a detrimental effect on the stainless steel container of the oxygen bomb. Consequently, the experimentally

determined heat of combustion for raw μ Al and $[n\text{Cu}+n\text{Ni}]/\mu\text{Al}$ was measured at merely $-24,988 \text{ kJ/kg}$ and $-21,952 \text{ kJ/kg}$, respectively, significantly lower than the theoretical heat of combustion for pure aluminum powder, which is $-31,000 \text{ kJ/kg}$. Nevertheless, the disparity in combustion heat between the two materials is negligible, with the combustion heat of $[n\text{Cu}+n\text{Ni}]/\mu\text{Al}$ being marginally less than that of μAl . This phenomenon can be attributed to the considerably lower combustion heats of copper (-2500 kJ/kg) and nickel (-4100 kJ/kg) in comparison to aluminum ($-31,000 \text{ kJ/kg}$), which consequently leads to a reduction in the overall combustion heat of $[n\text{Cu}+n\text{Ni}]/\mu\text{Al}$ relative to μAl . This observation underscores the validity and consistency of our experimental findings. Furthermore, upon evaluating the combustion heats of $\mu\text{Al}+\text{AP}$ and $[n\text{Cu}+n\text{Ni}]/\mu\text{Al}+\text{AP}$, it remains evident that the combustion heat of the latter is still slightly inferior to that of $\mu\text{Al}+\text{AP}$. The observed results can be attributed to the significantly lower combustion heat of copper and nickel in pure oxygen compared to that of aluminum. Furthermore, when ammonium perchlorate was employed as the primary oxidizer, the thermal output from the oxidation reactions of μAl and $[n\text{Cu}+n\text{Ni}]/\mu\text{Al}$ was markedly diminished in comparison to the heat release observed when utilizing pure oxygen as the oxidizing agent. This phenomenon arises from the differing characteristics of the oxidizers used and represents a typical occurrence in experimental contexts.

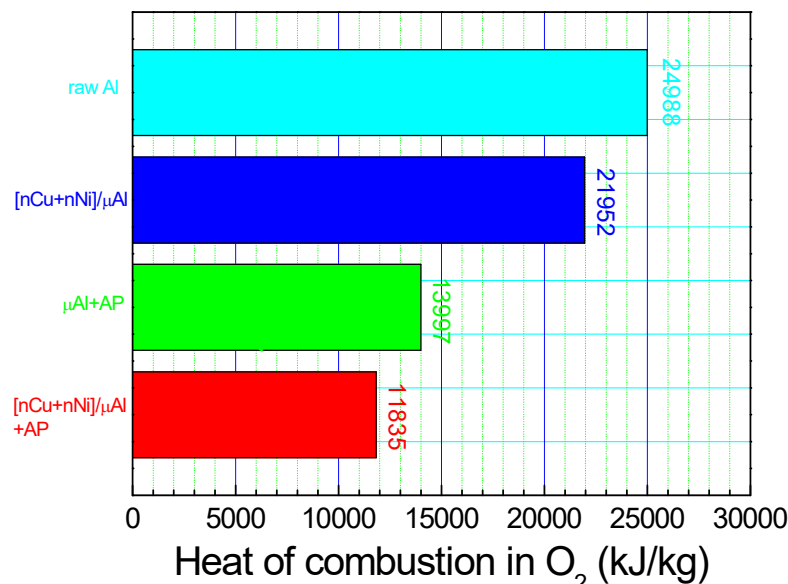


Figure 13. Heat release of combustion in pure and excessive oxygen.

3. Experimental Sections

3.1. Materials

Micro-aluminum powder (μAl , $d_{50} \approx 20 \mu\text{m}$, >98%), nickel chloride ($\text{NiCl}_2 \cdot 6\text{H}_2\text{O}$, C.P.), copper chloride ($\text{CuCl}_2 \cdot 6\text{H}_2\text{O}$, C.P.), EDTA-2Na ($\text{C}_{10}\text{H}_{14}\text{N}_2\text{Na}_2\text{O}_8$, C.P.), and ammonium fluoride (NH_4F , C.P.) were obtained from Sino Pharm of China. Ammonium perchlorate (NH_4ClO_4 , AP) was purchased from Gansu Yinguang Chemical Factory.

3.2. Preparation of $[n\text{Cu}+n\text{Ni}]/\mu\text{Al}$

Here, $[n\text{Cu}+n\text{Ni}]/\mu\text{Al}$ refers to the nanocomposite that the micron Al is coated with metallic nCu and nNi. The whole process was carried out at ambient temperature and pressure, and the preparation mechanism of $[n\text{Cu}+n\text{Ni}]/\mu\text{Al}$ is shown in Figure 14. Typically, a dense oxide layer is present on the surface of μAl particles, which is unavoidable. If this oxide layer is not broken, the metallic aluminum trapped inside cannot undergo a

displacement reaction with transition metal ions in the solution. Therefore, to successfully prepare $[n\text{Cu}+n\text{Ni}]/\mu\text{Al}$, the first step is to remove this alumina layer. In aqueous solutions, the substances that can rapidly dissolve alumina are strong acids and strong bases. However, while they dissolve the alumina layer, they also significantly corrode the metallic aluminum particles. After extensive experimentation, ammonium fluoride attracted our attention. Ammonium fluoride plays an important role in dissolving the aluminum oxide layer. In addition, as long as the concentration of ammonium fluoride is well controlled, it dissolves only the alumina layers in the solution without significantly corroding metallic aluminum. In particular, the fluoride ions in the solution can easily react with the alumina layer to form $[\text{AlF}_6]^{3-}$ ions, which are highly soluble in water, thus removing the oxide layer and allowing the displacement reaction between metallic aluminum and transition metal ions to proceed rapidly in weakly alkaline aqueous solutions.

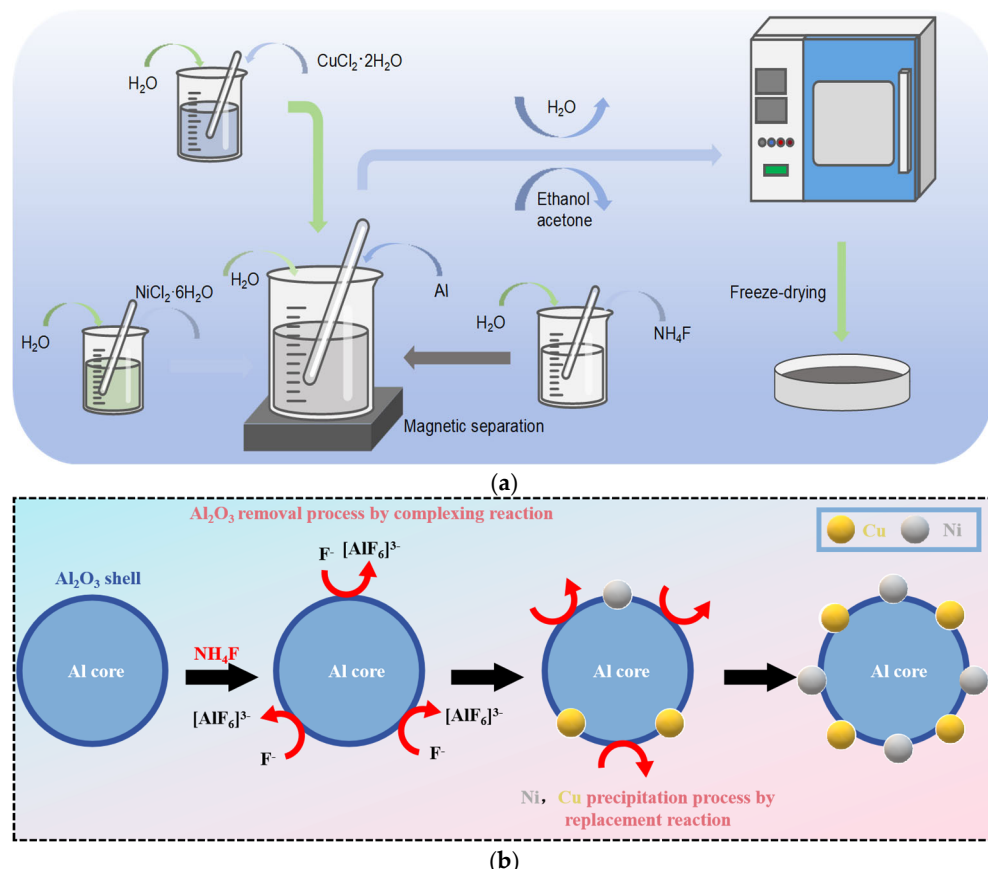


Figure 14. Schematic diagram of the preparation process of $[n\text{Cu}+n\text{Ni}]/\mu\text{Al}$: (a) preparation flowchart; (b) schematic of principle.

Initially, approximately 5 g of micro-aluminum (μAl , $d_{50} \approx 20 \mu\text{m}$) dry powder should be placed into an agate mortar, where it should be meticulously ground until there is no agglomerated μAl . Subsequently, 0.359 g of nickel(II) chloride hexahydrate ($\text{NiCl}_2 \cdot 6\text{H}_2\text{O}$) and 0.16 g of copper(II) chloride dihydrate ($\text{CuCl}_2 \cdot 2\text{H}_2\text{O}$), along with a minimal quantity of the complexing agent ethylenediaminetetraacetic acid disodium salt (EDTA-2Na), are to be dissolved in 15 mL of distilled water to yield a clear green solution. Following this, 2 g of crushed ice is introduced into the aforementioned solution, after which 1.5 g of the previously ground μAl is incorporated. Under vigorous stirring and the application of high-intensity ultrasound, a homogeneous suspension based on μAl is generated. Lastly, 0.5 g of ammonium fluoride (NH_4F) is dissolved in an additional 2 mL of distilled water to produce a colorless and transparent solution. This ammonium fluoride solution is then concurrently

added to the μAl -based suspension along with 3 g of crushed ice. Under conditions of stirring, yet devoid of ultrasound, a robust magnet was placed at the exterior bottom of the beaker after a duration of ten minutes. This strategic placement facilitated the adsorption of the μAl powder, which is coated with metallic nano-nickel (nNi) and nano-copper (nCu), to the beaker's base. Subsequently, the magnetically attracted materials were subjected to a washing process with distilled water (three times), followed by anhydrous ethanol (twice), and finally acetone (once). The resultant wet residual material was then filtered. Ultimately, the wet residue underwent freeze-drying utilizing a freeze dryer, yielding a dry powder composed of [nCu+nNi]/ μAl . This entire procedure for the preparation of the [nCu+nNi]/ μAl powder was conducted at ambient temperature, as depicted in Figure 14.

3.3. Characterization and Tests

Scanning Electron Microscope (SEM) images were taken using the TESCAN MIRA3, the elemental composition of the samples was checked using Energy Dispersive Spectroscopy (EDS) on the SEM, and the samples were gold sprayed using an ion sprayer to increase the conductivity of the samples prior to use. Empyrean X-Ray diffractometer (XRD) and X-Ray photoelectron spectroscopy (XPS) were used to characterize the phase and structural composition. The surface roughness and sphericity of the samples were characterized by an OLS5000 laser microscope. The exothermic reaction properties of the samples were studied by thermogravimetry and differential scanning calorimetry (TG-DSC). Differential scanning calorimetry (DSC, DSC-100) with heating rates of 5, 7, 10, and 15 °C/min was used to study the thermal decomposition of AP, and the sample masses were 5 mg. A high-speed camera was used in constant volume combustion tests (Shanghai Shuangxu Electronics Co., Ltd. Shanghai, China). The heat of combustion was measured using a fully automatic calorimeter (ZDHW-4). The thermal imager (HT30-300010001) was employed to measure and record the combustion flame temperature. The schematic diagram of the combustion performance testing device is shown in Figure 15. Thermal sensitivity tests (i.e., 5 s bursting point tests) were carried out in compliance with GJB772A-97 method 606.1; the quantitative sample was heated by the Wood alloy bath, and the sample responded after a delay.

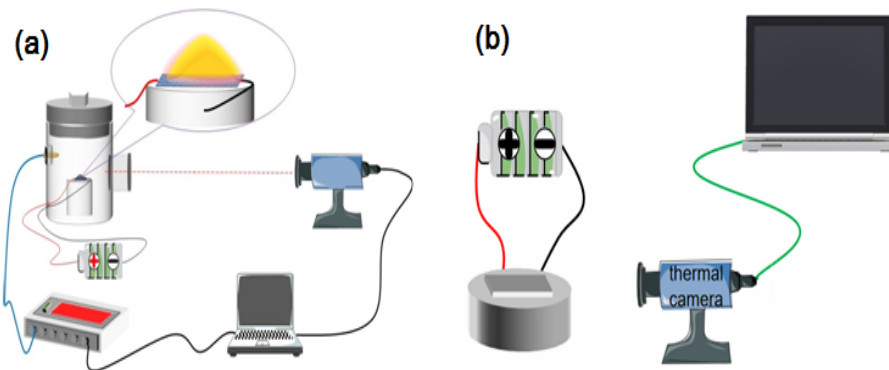


Figure 15. Diagram of combustion performance testing device: (a) constant volume combustion vessel; (b) constant pressure combustion device.

4. Conclusions

In this article, we report the successful dense coating of metallic copper and nickel nanoparticles onto the surface of micron-sized aluminum particles. Characterization results reveal that the nanoparticles adhering to the micron aluminum are, indeed, metallic copper and nickel. However, it should be noted that a minor fraction of the copper and nickel nanoparticles experienced oxidation during the preparation process. Furthermore, thermal analysis experiments demonstrated that the inclusion of copper and nickel nanoparticles

notably accelerated the oxidation of micron aluminum and significantly expedited the thermal decomposition of ammonium perchlorate. Notably, the activation energy for the thermal decomposition of ammonium perchlorate was markedly diminished, which serves as a promising indication of enhanced reactivity. Furthermore, we undertook a comprehensive investigation into the impacts of nanoparticulate copper and nickel on the combustion performance of micron aluminum and AP. The findings reveal that samples devoid of nano-copper (nCu) and nano-nickel (nNi) exhibit negligible ignitability when subjected to a hot wire, whereas the composite [nCu+nNi]/ μ Al+AP readily ignites and engages in vigorous combustion upon similar exposure. Furthermore, in our investigation of combustion heat, we observed that the combustion heat of the composite [nCu+nNi]/ μ Al was only marginally lower than that of μ Al itself. This finding suggests that the incorporation of nCu and nNi does not significantly impair the energetic performance of micro-aluminum. Collectively, these results illustrate that the nCu and nNi coated on the surface of micro-aluminum substantially enhance the decomposition, oxidation, and combustion kinetics of ammonium perchlorate and micro-aluminum. Consequently, [nCu+nNi]/ μ Al emerges as a superior fuel for solid propellants compared to pure micron aluminum.

Author Contributions: Y.W.: Data analysis and Writing; X.S.: Writing, Methodology, Formal analysis, Validation, and Supervision. All authors have read and agreed to the published version of the manuscript.

Funding: This research received no external funding.

Institutional Review Board Statement: This study was conducted in compliance with data protection regulations. The use of personal data was approved by the Ethics Committee of the North University of China Ethics Committee, ensuring that all data were anonymized and securely stored.

Data Availability Statement: All data generated or analyzed during this study are included in this article.

Acknowledgments: Thank you to Chongwei An and Fengsheng Li for their help with the software.

Conflicts of Interest: There are no conflicts of interest to declare.

References

1. Jackson, T.L.; Buckmaster, J.; Wang, X. Modeling of propellants containing ultrafine aluminum. *J. Propuls. Power* **2007**, *23*, 158–165.
2. Yuan, J.F.; Liu, J.Z.; Zhou, Y.N.; Wang, J.; Xv, T. Aluminum agglomeration of AP/HTPB composite propellant. *Acta Astronaut.* **2019**, *156*, 14–22.
3. Gautham, M.G.; Ramakrishna, P.A. Combustion characteristics of aluminum-water gelled composite propellant. *J. Propuls. Power* **2018**, *34*, 1345–1353.
4. Gottfried, J.L.; Smith, D.K.; Wu, C.C.; Pantoya, M.L. Improving the explosive performance of aluminum nanoparticles with aluminum iodate hexahydrate (AIH). *Sci. Rep.* **2018**, *8*, 8036.
5. Pourmortazavi, S.M.; Hajimirsadeghi, S.S.; Kohsari, I.; Fathollahi, M.; Hosseini, S. Thermal decomposition of pyrotechnic mixtures containing either aluminum or magnesium powder as fuel. *Fuel* **2008**, *87*, 244–251.
6. Li, C.D.; Pi, Z.L.; Wang, F.; Wu, Y. Pore structure regulation of aluminum powder as a filler for high energy solid propellants. *Mater. Chem. Phys.* **2024**, *314*, 128911.
7. Makhov, M.N. Effect of aluminum and boron additives on the heat of explosion and acceleration ability of high explosives. *Russ. J. Phys. Chem. B* **2015**, *9*, 50–55.
8. Cudzilo, S.; Trzcinski, W.A.; Paszula, J.; Szala, M.; Chylek, Z. Performance of magnesium, Mg-Al alloy and silicon in thermobaric explosives—A comparison to aluminium. *Propellant Explos. Pyrotech.* **2020**, *45*, 1691–1697.
9. Azhagurajan, A.; Selvakumar, N.; Thanulingam, T.L. Thermal and sensitivity analysis of nano aluminium powder for firework application. *J. Therm. Anal. Calorim.* **2011**, *105*, 259–267.
10. Han, Z.Y.; Jiang, Q.; Du, Z.M.; Hoon, H.H.; Yu, Y.; Zhang, Y.; Li, G.; Sun, Y. A novel environmental-friendly and safe unpacking powder without magnesium, aluminum and sulphur for fireworks. *J. Hazard. Mater.* **2019**, *373*, 835–843.
11. Pantoya, M.L.; Granier, J.J. The effect of slow heating rates on the reaction mechanisms of nano and micron composite thermite reactions. *J. Therm. Anal. Calorim.* **2006**, *85*, 37–43. [[CrossRef](#)]

12. Trunov, M.A.; Schoenitz, M.; Zhu, X.Y.; Dreizin, E.L. Effect of polymorphic phase transformations in Al_2O_3 film on oxidation kinetics of aluminum powders. *Combust. Flame* **2005**, *140*, 310–318.
13. Jeurgens, L.P.H.; Sloof, W.G.; Tichelaar, F.D.; Mittemeijer, E. Composition and chemical state of the ions of aluminium-oxide films formed by thermal oxidation of aluminum. *Surf. Sci.* **2002**, *506*, 313–332.
14. Sánchez-López, J.C.; Fernández, A.; Conde, C.F.; Conde, A.; Morant, C.; Sanz, J. The melting behavior of passivated nanocrystalline aluminum. *Nanostruct. Mater.* **1996**, *7*, 813–822.
15. Wang, S.X.; Liang, K.M.; Zhang, X.H.; Wang, G.-L. Influence of heating-rate on DTA curve of the aluminothermic reaction. *J. Mater. Sci. Lett.* **2003**, *22*, 855–856.
16. Schoenitz, M.; Ward, T.S.; Dreizin, E.L. Fully dense nano-composite energetic powders prepared by arrested reactive milling. *Proc. Combust. Inst.* **2005**, *30*, 2071–2078.
17. Kim, K.T.; Kim, D.; Kim, C.K.; Choi, Y.J. A facile synthesis and efficient thermaloxidation of polytetrafluoroethylene-coated aluminum powders. *Mater. Lett.* **2016**, *167*, 262–265.
18. Guo, L.G.; Song, W.L.; Xie, C.S.; Zhang, X.; Hu, M. Characterization and thermalproperties of carbon-coated aluminum nanopowders prepared by laser-induction complex heating in methane. *Mater. Lett.* **2007**, *61*, 3211–3214.
19. Lyu, J.Y.; Chen, S.W.; He, W.; Zhang, X.X.; Tang, D.Y.; Liu, P.J.; Yan, Q.L. Fabrication of high-performancegraphene axidle doped PVDF/CuO/Al nanocomposites via electrospinning. *Chem. Eng.* **2019**, *368*, 129–137.
20. Zhou, H.; Lv, B.L.; Wu, D.; Xu, Y. Synthesis of polycrystalline Co_3O_4 nanowires with excellent ammonium perchlorate catalytic decompositionproperty. *Mater. Res. Bull.* **2014**, *60*, 492–497.
21. Cheng, Z.P.; Chu, X.Z.; Yin, J.Z.; Dai, B.; Zhao, W.; Jiang, Y.; Xu, J.; Zhong, H.; Zhao, P.; Zhang, L. Formation of compositefuels by coating aluminum powder with a cobalt nanocalalyst: Enhanced heat release and catalytic performance. *Chem. Eng.* **2020**, *385*, 123859.
22. Cheng, Z.P.; Chu, X.Z.; Zhao, W.; Yin, J.; Dai, B.; Zhong, H.; Xu, J.; Jiang, Y. Controllable synthesis of Cu/Al energetic nanocomposites with excellent heat release and combustion performance. *Appl. Surf. Sci.* **2020**, *513*, 145704.
23. Liu, L.L.; Li, F.S.; Tan, L.; Ming, L.; Yi, Y. Effects of nanometer Ni, Cu, Al and NiCu powders on the thermal decomposition of ammonium perchlorate. *Propellants Explos. Pyrotech.* **2004**, *29*, 34–38.
24. Song, M.R.; Chen, M.; Zhang, Z.J. Effect of Zn powders on the thermal decomposition of ammonium perchlorate. *Propellants Explos. Pyrotech.* **2008**, *33*, 261–265.
25. Yan, J.; Wang, H.; Jin, B.; Zeng, M.; Peng, R. Cu-MOF derived Cu/ Cu_2O /C nanocomposites for the efficient thermal decomposition of ammonium perchlorate. *J. Solid State Chem.* **2021**, *297*, 122060.
26. Duan, H.Z.; Lin, X.Y.; Liu, G.P.; Li, F.S. Synthesis of Co nanoparticles and their catalytic effect on the decomposition of ammonium perchlorate. *Chin. J. Chem. Eng.* **2008**, *16*, 325–328.
27. Duan, H.Z.; Lin, X.Y.; Liu, G.P.; Xu, L.; Li, F.S. Synthesis of Ni nanoparticles and their catalytic effect on the decomposition of ammonium perchlorate. *J. Mater. Process. Technol.* **2008**, *208*, 494–498.
28. Kou, Y.; Wang, Y.; Zhang, J.; Guo, K.G.; Song, X.L. Iron/aluminum nanocomposites prepared by one-step reduction method and their effects on thermal decomposition of AP and AN. *Def. Technol.* **2023**, *22*, 74–87. [CrossRef]
29. Wang, Y.; Jiang, W.; Cheng, Z.P.; Chen, W.F.; An, C.; Song, X.; Li, F. Thermite reaction of Al/Cu core-shell nanocomposites with WO_3 . *Thermochim. Acta* **2007**, *463*, 69–76.
30. Wang, Y.; Song, X.L.; Jiang, W.; Deng, G.D.; Guo, X.D.; Liu, H.Y.; Li, F.S. Synthesis of nano-nickel-coated micro-aluminum and thermal reactivity of aluminum/nickel stannic-oxide thermite. *Int. J. Energetic Mater. Chem. Propuls.* **2011**, *10*, 231–243.
31. Zi, R.C.; Han, Z.Y.; Yu, Y.; Wang, C.; Zhang, X.; Guo, X.; Chen, J.; Zhang, X.; Yang, J. Properties of mixed crystal coprecipitation substances of ammonium nitrate and potassium perchlorate prepared by the evaporative solvent method. *ACS Omega* **2023**, *9*, 1573–1590. [PubMed]
32. Wang, Y.; Song, X.I.; Li, F.S. Thermal behavior and decomposition mechanism of ammonium perchlorate and ammonium nitrate in the presence of nanometer triaminoguanidine nitrate. *ACS Omega* **2019**, *4*, 214–225. [PubMed]
33. Lee, D.G.; Lee, C.J. Fuel-Rich combustion with ammonium perchlorate addition in a staged hybrid rocket engine. *J. Propuls. Power* **2017**, *33*, 1581–1588.
34. Zhou, L.Y.; Cao, S.B.; Zhang, L.L.; Xiang, G.; Wang, J.; Zeng, X.; Chen, J. Facet effect of Co_3O_4 nanocatalysts on the catalytic decomposition of ammonium perchlorate. *J. Hazard. Mater.* **2020**, *392*, 122358.
35. Vara, J.A.; Dave, P.N.; Chaturvedi, S. Investigating catalytic properties of nanoferrites for both AP and nano-AP based composite solid propellant. *Combust. Sci. Technol.* **2021**, *193*, 2290–2304.
36. Song, X.L.; Wang, Y.; Song, D.; An, C.; Wang, J. Catalysis of a nanometer solid super acid of $\text{SO}_4^{2-}/\text{TiO}_2$ on the thermal decomposition of ammonium nitrate. *Nanomater. Nanotechnol.* **2016**, *6*, 23. [CrossRef]
37. Song, X.L.; Wang, Y.; Song, D.; An, C.; Wang, J. Thermal decomposition of ammonium perchlorate and ammonium nitrate doped with nanometer $\text{SO}_4^{2-}/\text{Fe}_2\text{O}_3$ solid strong acid as catalyst. *Sci. Technol. Energetic Mater.* **2016**, *77*, 65–71.

38. Wang, Y.; Song, X.L.; Li, F.S. Nanometer ammonium perchlorate and ammonium nitrate with 2D network structure prepared via rapid freezing technology. *Nanomaterials* **2019**, *9*, 1605.
39. Meng, S.H.; Liu, J.F.; Kong, X.T.; Du, S.G. Preparation of TiO₂/CNTs nanocomposite and its catalytic performance on the thermal decomposition of ammonium perchlorate. *Transit. Met. Chem.* **2020**, *45*, 545–551.
40. Hu, Y.H.; Tao, B.; Shang, F.; Zhou, M.X.; Hao, D.; Fan, R.; Xia, D.; Yang, Y.; Pang, A.; Lin, K. Thermal decomposition of ammonium perchlorate over perovskite catalysts: Catalytic decomposition behavior, mechanism and application. *Appl. Surf. Sci.* **2020**, *513*, 145849.
41. Carignan, L.P.; Lacroix, C.; Ouimet, A.; Ciureanu, M.; Yelon, A.; Ménard, D. Magnetic anisotropy in arrays of Ni, CoFeB, and Ni/Cu nanowires. *J. Appl. Phys.* **2007**, *102*, 023905. [[CrossRef](#)]
42. Rani, B.J.; Saravanan Kumar, B.; Ravi, G.; Ganesh, V.; Sakunthala, A.; Yuvakkumar, R. Structural, optical and magnetic properties of NiO nanopowders. *J. Nanosci. Nanotechnol.* **2018**, *18*, 4658–4666. [[PubMed](#)]
43. Liu, X.S.; Hu, F.; Zhu, D.R.; Jia, D.N.; Wang, P.-P.; Ruan, Z.; Cheng, C.-H. One-step synthesis of carbon nanotubes with Ni nanoparticles as a catalyst by the microwave-assisted polyol method. *J. Alloys Compd.* **2011**, *509*, 2829–2832.
44. Chen, L.J.; Li, G.S.; Qi, P.; Li, L.O. Thermal decomposition of ammonium perchlorate activated via addition of NiO nanocrystals. *J. Therm. Anal. Calorim.* **2008**, *92*, 765–769.
45. Chen, L.J.; Li, G.S.; Li, L.O. CuO nanocrystals in thermal decomposition of ammonium perchlorate. *J. Therm. Anal. Calorim.* **2008**, *91*, 581–587.
46. Li, J.W.; Li, J.F.; Zhang, D.X.; Wu, B.D. Preparation of Micron-scale DAP-4-based Energetic Composite Microspheres by Microfluidic Technology and its Characterization. *Chin. J. Energ. Mater.* **2024**, *32*, 249–255.
47. Shi, J.H.; Wu, B.D.; Zhou, J.Q.; Ren, D.W. One-step rapid preparation of CL-20/TNT co-crystal assembly and spheroidized coating based on droplet microfluidic technology. *Def. Technol.* **2023**, *27*, 251–262.
48. Guo, Y.Y.; Liu, Y.; Guan, Q. Preparation of micron-sized ammonium perchlorate with narrow particle size distribution based on microfluidic technology. *Initiat. Pyrotech.* **2024**, *33*–39.
49. Zhang, T.T.; Jiang, Y.Q.; Huo, W.L. Preparation and combustion properties of AP@Al composites. *Solid Rocket. Technol.* **2024**, *47*, 1–13.
50. Kissinger, H.E. Reaction kinetics in differential thermal analysis. *Anal. Chem.* **1957**, *29*, 1702–1706.
51. Han, Z.W.; Han, Y.C.; Xu, S. Preparation of nano-cerium dioxide and its effect on the thermal decomposition of ammonium perchlorate. *J. Therm. Anal. Calorim.* **2014**, *116*, 273–278. [[CrossRef](#)]
52. Fujimura, K.; Miyake, A. The effect of specific surface area of TiO₂ on the thermal decomposition of ammonium perchlorate. *J. Therm. Anal. Calorim.* **2010**, *99*, 27–31. [[CrossRef](#)]
53. Shim, H.M.; Lee, E.A.; Kim, J.K. Formation of tungsten/ammonium perchlorate composites and their reaction kinetics. *Cent. Eur. J. Energ. Mater.* **2015**, *12*, 703–722.
54. Song, Y.; Song, X.L.; Song, D.; Liang, L.; An, C.; Wang, J. Synthesis, thermolysis, and sensitivities of HMX/NC energetic nanocomposites. *J. Hazard. Mater.* **2016**, *312*, 73–83. [[CrossRef](#)]
55. Yu, Z.H.; Song, X.L.; Kou, Y.; Wang, Y.; An, C. Characterization and testing for lowest eutectic mixture of TNBA/DNTF. *Propellants Explos. Pyrotech.* **2023**, *48*, e202200201. [[CrossRef](#)]
56. Dong, C.; Wang, Y.; Jia, K.H.; Song, D.; Song, X.; An, C. Preparation and characterization of high-reactivity explosive-based nano-boron microspheres. *Particuology* **2024**, *93*, 125–136. [[CrossRef](#)]

Disclaimer/Publisher’s Note: The statements, opinions and data contained in all publications are solely those of the individual author(s) and contributor(s) and not of MDPI and/or the editor(s). MDPI and/or the editor(s) disclaim responsibility for any injury to people or property resulting from any ideas, methods, instructions or products referred to in the content.

Reproduced with permission of copyright owner. Further reproduction
prohibited without permission.